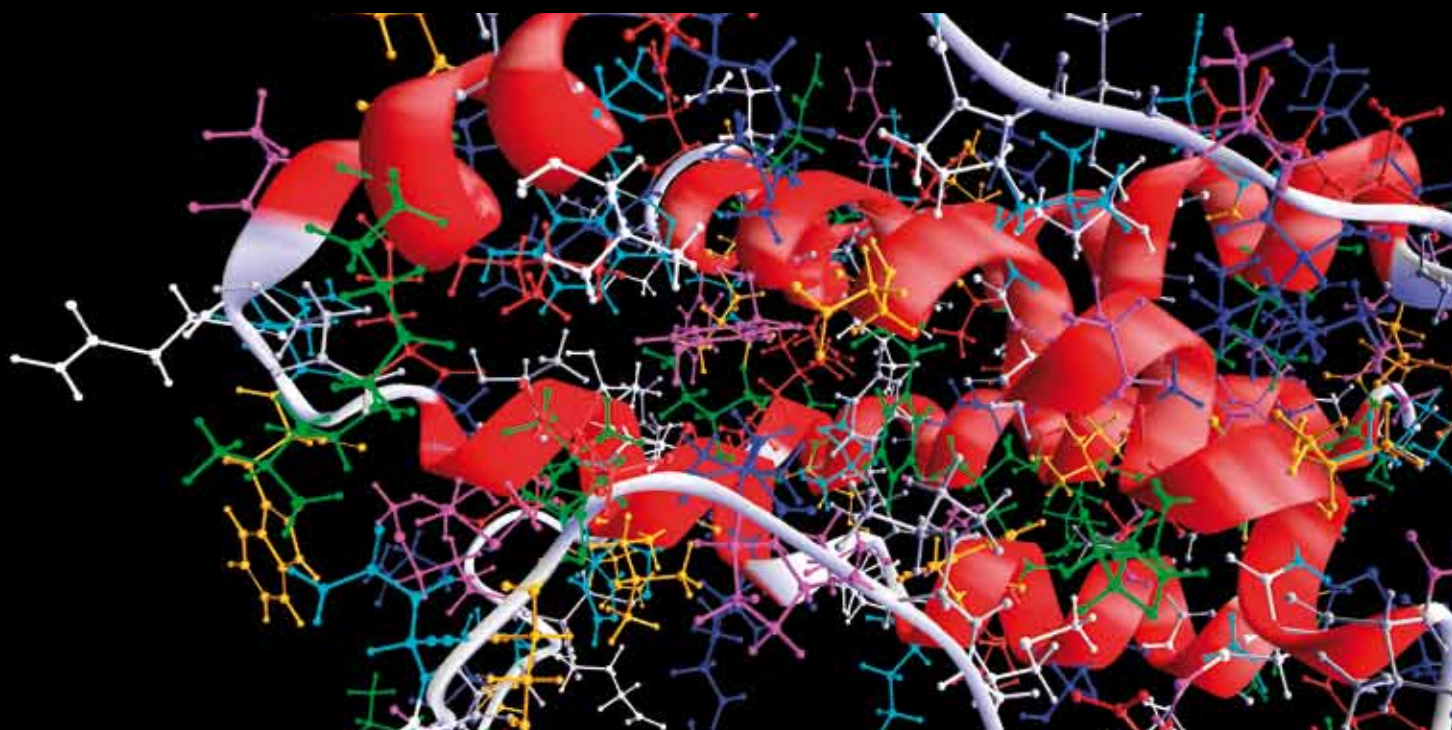


COMPUTATIONAL AND MATHEMATICAL METHODS IN MEDICINE

COMPUTATIONAL METHODOLOGY of OPTICAL MOLECULAR IMAGING

GUEST EDITORS: CHENGHU QIN, YUJIE LU, JIMIN LIANG, DEMING KONG, AND HUADAN XUE





Computational Methodology of Optical Molecular Imaging

Computational and Mathematical Methods in Medicine

Computational Methodology of Optical Molecular Imaging

Guest Editors: Chenghu Qin, Yujie Lu, Jimin Liang,
Deming Kong, and Huadan Xue



Copyright © 2013 Hindawi Publishing Corporation. All rights reserved.

This is a special issue published in “Computational and Mathematical Methods in Medicine.” All articles are open access articles distributed under the Creative Commons Attribution License, which permits unrestricted use, distribution, and reproduction in any medium, provided the original work is properly cited.

Editorial Board

Emil Alexov, USA
Georgios Archontis, Cyprus
Dimos Baltas, Germany
Chris Bauch, Canada
Maxim Bazhenov, USA
Thierry Busso, France
Carlo Cattani, Italy
William Crum, UK
Ricardo Femat, Mexico
Alfonso T. Garía-Sosa, Estonia
Damien R. Hall, Japan

Volkhard Helms, Germany
Seiya Imoto, Japan
Lev Klebanov, Czech Republic
Quan Long, UK
C-M Charlie Ma, USA
Reinoud Maex, France
Simeone Marino, USA
Michele Migliore, Italy
Karol Miller, Australia
Ernst Niebur, USA
Kazuhisa Nishizawa, Japan

Hugo Palmans, UK
David James Sherman, France
Sivabal Sivaloganathan, Canada
Nestor V. Torres, Spain
Nelson J. Trujillo-Barreto, Cuba
Gabriel Turinici, France
Kutlu O. Ulgen, Turkey
Edelmira Valero, Spain
Jacek Waniewski, Poland
Guang Wu, China
Henggui Zhang, United Kingdom

Contents

Computational Methodology of Optical Molecular Imaging, Chenghu Qin, Yujie Lu, Jimin Liang, Deming Kong, and Huadan Xue
Volume 2013, Article ID 432107, 1 page

Retinal Image Graph-Cut Segmentation Algorithm Using Multiscale Hessian-Enhancement-Based Nonlocal Mean Filter, Jian Zheng, Pei-Rong Lu, Dehui Xiang, Ya-Kang Dai, Zhao-Bang Liu, Duo-Jie Kuai, Hui Xue, and Yue-Tao Yang
Volume 2013, Article ID 927285, 7 pages

A New Multichannel Spectral Imaging Laser Scanning Confocal Microscope, Yunhai Zhang, Bian Hu, Yakang Dai, Haomin Yang, Wei Huang, Xiaojun Xue, Fazhi Li, Xin Zhang, Chenyu Jiang, Fei Gao, and Jian Chang
Volume 2013, Article ID 890203, 8 pages

Hybrid Multilevel Sparse Reconstruction for a Whole Domain Bioluminescence Tomography Using Adaptive Finite Element, Jingjing Yu, Xiaowei He, Guohua Geng, Fang Liu, and L. C. Jiao
Volume 2013, Article ID 548491, 12 pages

Morphological Measurement of Living Cells in Methanol with Digital Holographic Microscopy, Yunxin Wang, Yishu Yang, Dayong Wang, Liting Ouyang, Yizhuo Zhang, Jie Zhao, and Xinlong Wang
Volume 2013, Article ID 715843, 7 pages

Improved Reconstruction Quality of Bioluminescent Images by Combining SP_3 Equations and Bregman Iteration Method, Qiang Wu, Jinchao Feng, Kebin Jia, and Xiangyu Wang
Volume 2013, Article ID 767296, 8 pages

Editorial

Computational Methodology of Optical Molecular Imaging

Chenghu Qin,¹ Yujie Lu,² Jimin Liang,³ Deming Kong,⁴ and Huadan Xue⁵

¹ Chinese Academy of Sciences, Beijing 100864, China

² Center for Molecular Imaging, University of Texas Health Science Center at Houston, Houston, TX 77030, USA

³ School of Life Science and Technology, Xidian University, Xi'an, Shaanxi 710071, China

⁴ College of Chemistry, Nankai University, Tianjin 300071, China

⁵ Department of Radiology, Union Hospital, Chinese Academy of Medical Sciences and Peking, Union Medical College, Beijing 100730, China

Correspondence should be addressed to Chenghu Qin; chqin@cashq.ac.cn

Received 8 September 2013; Accepted 8 September 2013

Copyright © 2013 Chenghu Qin et al. This is an open access article distributed under the Creative Commons Attribution License, which permits unrestricted use, distribution, and reproduction in any medium, provided the original work is properly cited.

Molecular imaging emerging in the early 21st century has been rapidly developed. Over more than 10 years, optical molecular imaging has become an important tool in pre-clinical research and has been translated into the clinical for clinical diagnosis and therapy. Computational methodology has shown its indispensable position in developing molecular probes, building imaging instruments, researching reconstruction algorithms, and studying signal and image processing. Relevant research not only adapts existing computational methods but also develops novel strategies to tackle with challenging problems in optical molecular imaging.

This special issue is devoted to the topic of computational algorithms and strategies in optical molecular imaging. Five exciting papers assembled in this special issue present a common theme, that is, improving the imaging and image processing performance in optical molecular imaging by using computational techniques. The papers address several problems in optical molecular imaging, including optical tomographic reconstruction for bioluminescence tomography and image processing such as image segmentation, 3D rendering, and cell morphological measurements. In detail, J. Yu et al. make use of a hybrid multilevel adaptive finite element reconstruction scheme and sparse regularization to acquire quantitative information of bioluminescent sources. The work of Q. Wu et al. is to take advantage of a high-order photon propagation model and Bregman optimization algorithm to improve bioluminescence tomography. The morphology information of living cells and 3D tissue

images at the micrometer level can be obtained by using existing computational algorithms from the developed digital holographic microscopy and multichannel spectral imaging laser scanning confocal microscope in the research progress of Y. Wang et al. and Y. Zhang et al., respectively. J. Zheng et al. report that retinal vessels are also efficiently extracted with multiscale hessian-enhancement-based nonlocal mean filter.

Acknowledgments

We hope that this exciting special issue highlights some of the current efforts to use sophisticated computational methods to solve the challenges in optical molecular imaging. We believe that relevant progress can propel the development of efficiently solving relevant problems. We would like to thank all the anonymous reviewers for their time and efforts and the publishing office for making a timely production schedule.

Chenghu Qin
Yujie Lu
Jimin Liang
Deming Kong
Huadan Xue

Research Article

Retinal Image Graph-Cut Segmentation Algorithm Using Multiscale Hessian-Enhancement-Based Nonlocal Mean Filter

Jian Zheng,¹ Pei-Rong Lu,² Dehui Xiang,³ Ya-Kang Dai,¹ Zhao-Bang Liu,¹
Duo-Jie Kuai,¹ Hui Xue,¹ and Yue-Tao Yang¹

¹ Suzhou Institute of Biomedical Engineering and Technology, Chinese Academy of Sciences, Suzhou 215163, China

² Department of Ophthalmology, The First Affiliated Hospital of Soochow University, Suzhou 215006, China

³ Institute of Automation, Chinese Academy of Sciences, Beijing 100190, China

Correspondence should be addressed to Jian Zheng; zhengj@sibet.ac.cn

Received 4 January 2013; Accepted 25 March 2013

Academic Editor: Yujie Lu

Copyright © 2013 Jian Zheng et al. This is an open access article distributed under the Creative Commons Attribution License, which permits unrestricted use, distribution, and reproduction in any medium, provided the original work is properly cited.

We propose a new method to enhance and extract the retinal vessels. First, we employ a multiscale Hessian-based filter to compute the maximum response of vessel likeness function for each pixel. By this step, blood vessels of different widths are significantly enhanced. Then, we adopt a nonlocal mean filter to suppress the noise of enhanced image and maintain the vessel information at the same time. After that, a radial gradient symmetry transformation is adopted to suppress the nonvessel structures. Finally, an accurate graph-cut segmentation step is performed using the result of previous symmetry transformation as an initial. We test the proposed approach on the publicly available databases: DRIVE. The experimental results show that our method is quite effective.

1. Introduction

The retina is the only tissue in human body from which the information of blood vessel can be directly obtained in vivo. The information of retinal vessel plays an important role in the diagnosis and treatment of various diseases such as glaucoma [1], age-related macular degeneration [2], degenerative myopia, and diabetic retinopathy [3]. Recently, it is also found that the detection of vascular geometric change might be meaningful to judge whether people have high blood pressure or cardiovascular disease [4]. Retinal vessel extraction is quite essential for ophthalmologists to diagnose various eye diseases. Moreover, accurately segmented vessels could be very helpful for feature-based retinal image registration.

Generally, existing retinal vessel segmentation methods can be roughly divided into two categories. The first category is supervised learning-based method. Such methods require tremendous manual segmentations of vasculature to train the classifier. Staal et al. [5] first adopt a ridge-extraction method to separate the image into numerous patches. For each pixel in the patch, feature vector that contains profile information such as width, height, and edge strength is computed. Feature vectors are then classified using a k nearest neighbors classifier with sequential forward feature

selection strategy. Soares et al. [6] selected pixel value and multiscale 2D Gabor wavelet coefficients to construct the feature vector. A Bayesian classifier based on class-conditional probability density functions was adopted to perform a fast classification and model complex decision surfaces. Marín et al. [7] proposed a new supervised method to segment retinal vessels. For each pixel, 5 gray-level descriptors and 2 moment invariants-based features of a squared window were computed as the feature vector. A multilayer neural network scheme was then adopted to classify each pixel. The performance of such method depends on the correlation between training data and test data. If these two datasets are quite different, the segmentation results may be less than ideal. Besides that, the manual segmentation step would bring additional burden to ophthalmologists. Therefore, such methods have not been widely used in clinic yet.

The second category is rule-based method. Such methods usually need to extract neighborhood information of each pixel. The information is then used to label the pixel according to some f preset rules. Matched filter [8], model-based method [9], and morphology-based method [10] all belong to this category. In the literature [8], Sofka and Stewart proposed a multiscale Gaussian and Gaussian-derivative profile kernel

to detect vessels at a variety of widths. Lam et al. [9] proposed a multiconcavity modeling approach to handle unhealthy retinal images. In Lam's approach, a lineshape concavity measure was used to remove dark lesions and a locally normalized concavity measure is designed to remove spherical intensity variation. The two concavity measures are combined together according to their statistical distributions to detect vessels in general retinal images. Mendonça and Campilho [10] proposed a region growing algorithm in the morphological processed image to extract vascular centerline. First, four-direction-based differential operator was adopted to detect vascular centerlines. These centerlines were then merged to complete vascular centerlines and selected as seed points. Finally, region growing step was performed to reconstruct the vasculature. These methods do not require training steps and the interactions with doctors are also minimized; thus rule-based methods have been widely used in clinical application. However, ideal automatic retinal vessel segmentation is still not easy. This can mainly be ascribed to two reasons. One is that the contrast of some tiny vessels may be quite low, especially in some pathologies affected images. The other reason is that the image noise such as edge blurring may disturb the final segmentation results.

Recently, graph-cut methods [11–15] have been very popular in image segmentation. This is because graph-cut methods could reach the global optimal value of the pre-defined energy function. Besides that, the user interactions of such methods are also very simple. Several graph-cut-based methods have been proposed to solve retina image segmentations. Chen et al. [16] proposed a 3D graph-search-graph-cut method to segment multilayers of 3D OCT retinal images. The multi-layers of retina and the symptomatic exudate-associated derangements (SEAD) are successfully segmented. Inspired by the superior performance of graph-cut method, we propose a new method to extract the blood vessels in retinal images following our previous work [17]. First, we perform a novel multiscale Hessian-based filter to compute the maximum response of vessel likeness function for each pixel, which is used to enhance the blood vessels of gray retinal images. Then, we adopt a nonlocal mean filter to suppress the noise of the enhanced image. After that, a radial gradient symmetry transformation is adopted to improve the detection of vessel structures and suppress the nonvessel structures. Finally, an accurate graph-cut segmentation is performed using previous symmetry transformation as an initial.

2. Methods

2.1. Multiscale Hessian-Based Enhancement. In order to improve the contrast of retinal vasculature with different widths, we propose a multiscale Hessian-based enhancement. Frangi et al. [18] have proposed a method to detect the tubular structure based on the eigenvalues of Hessian matrix. We denote by $\lambda_{1,s}$ and $\lambda_{2,s}$ the eigenvalues of scale-related Hessian matrix, which is defined as follows:

$$H(X, s) = \begin{bmatrix} I_{xx}(X, s) & I_{xy}(X, s) \\ I_{yx}(X, s) & I_{yy}(X, s) \end{bmatrix}, \quad (1)$$

where $I_{xx}(X, s)$ is the second order differential of input image. For an ideal tubular structure, the eigenvalues generally will meet the following conditions:

$$\begin{aligned} |\lambda_{1,s}| &\approx 0, \\ |\lambda_{1,s}| &\ll |\lambda_{2,s}|. \end{aligned} \quad (2)$$

We then define a new scale-related vessel likeness function:

$$VL(X) = \max_{s_{\min} < s < s_{\max}} V(s), \quad (3)$$

where $V(s)$ is defined as follow:

$$\begin{aligned} V(s) = & \frac{|\lambda_{1,s}|}{2} \cdot e^{c - (|\lambda_{1,s}| / \sqrt{\lambda_{1,s}^2 + \lambda_{2,s}^2})} \\ & + \frac{|\lambda_{2,s}|}{2} \cdot e^{(|\lambda_{2,s}| / \sqrt{\lambda_{1,s}^2 + \lambda_{2,s}^2}) - c}, \end{aligned} \quad (4)$$

where c is an experiential parameter and we set it to $\sqrt{2}/2$.

The function value of $V(s)$ indicates the saliency of tubular structure for each pixel. We search in the scale range $[s_{\min}, s_{\max}]$ to find the maximum response of vessel likeness function. Figure 2 shows the optimal scale property of the input image. The pixel value stands for the scale that is corresponding to the maximal function value of $V(s)$. As seen from Figure 2, the positive correlation between vessel width and optimal scale is obvious. The primary vessel owns a large scale property while the tiny vessel owns a small scale property.

Figure 3 gives an example of multiscale Hessian-based enhancement, in which the pixel value stands for the vessel likeness function value. As shown in Figure 3, the whole retinal vasculature is prominently enhanced. However, some nonvessel structures are also enhanced including optic disk, yellow spots, and speckles. These nonvessel structures need to be removed in the following step.

2.2. Nonlocal Mean Filtering. The effect of multiscale hessian based enhancement is obvious. As shown in Figure 3, the whole vasculature is significantly strengthened. However, some nonvessel structures are also enhanced and cause the enhanced image to be noisy. In order to suppress image noise and maintain the structural information, we employ a nonlocal mean filtering [19] step. We denote the enhanced image as $VL(X)$ and the filtered image as $NL(X)$. The detailed filtering step can be described as in the following equation:

$$NL(i) = \sum_{j \in N} w(i, j) \cdot VL(j), \quad (5)$$

where N denotes the filtering neighborhood and $w(i, j)$ is the weighting factor, which is defined as follow:

$$\begin{aligned} w(i, j) = & \frac{1}{Z(i)} \cdot \exp\left(-\frac{\|v(N_i) - v(N_j)\|^2}{h^2}\right), \\ Z(i) = & \sum_j \exp\left(-\frac{\|v(N_i) - v(N_j)\|^2}{h^2}\right), \end{aligned} \quad (6)$$



FIGURE 1: An example of an input retinal image, downloaded from publicly available databases: DRIVE (<http://www.isi.uu.nl/Research/Databases/DRIVE/>).

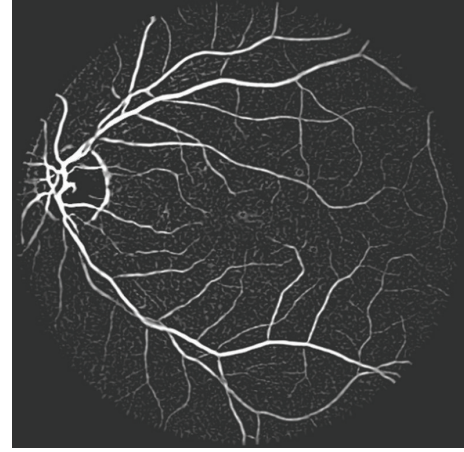


FIGURE 3: An example of the multiscale Hessian-based enhancement of Figure 1; the pixel value stands for the vessel likeness function value.

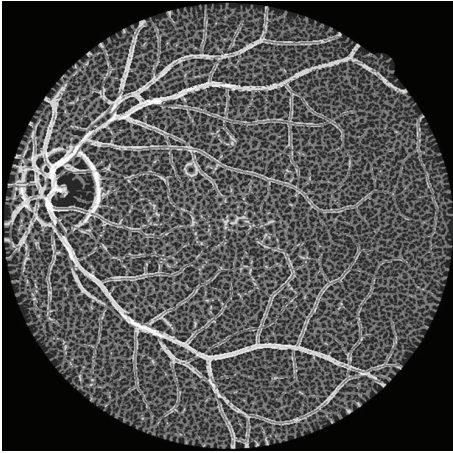


FIGURE 2: An example of the scale image of Figure 1; the pixel value stands for the scale that is corresponding to the maximal function value of $V(s)$.



FIGURE 4: An output of the nonlocal mean filter of Figure 3, in which the image noise is effectively suppressed while the vasculature is maintained.

where $v(N_i)$ denotes a feature vector which is composed of the pixel values of the nearby area around pixel i and h is a filtering parameter. The parameters of filtering neighborhood and nearby area need to be selected suitably so as to achieve a balance between filtering performance and computation cost. Figure 4 shows a result of nonlocal mean filtering. We can find that the noise of enhanced image is suppressed effectively while the vasculature is maintained at the same time.

2.3. Radial Gradient Symmetry Transform. In order to remove the nonvessel structures, we propose a radial gradient symmetry transform method based on Loy's work [20]. An ideal vessel structure is shown in Figure 5. As shown in Figure 5, we notice that the gradient vectors own a symmetric property in both the magnitude and direction. For those nonvessel structures, there is no such property. Therefore, we propose a symmetric vessel likeness function as follows:

$$VL_{\text{Sym}}(X) = VL_G(X) \cdot \text{Flag}_G(X), \quad (7)$$

where $VL_G(X)$ stands for a vessel likeness function of a given point X along the direction of gradient vector $G(X)$ and $\text{Flag}_G(X)$ is an indicator function that indicates whether point X owns the gradient symmetric property. The computation of $VL_G(X)$ and $\text{Flag}_G(X)$ consists of the following steps.

- (1) For each pixel in the filtered image as shown in Figure 4, we compute its vessel contribution along the gradient direction. The normalized gradient vector is denoted by $g(X) = G(X)/\|G(X)\|$. The coordinates of pixels that are affected by pixel p are computed as follows:

$$c(p) = p + \text{round}(r \cdot g(p)), \quad (8)$$

where $r = 0, \Delta r, \dots, 2 \cdot s(p)$ and $s(p)$ is the optimal scale parameter of pixel p , as shown in Figure 2.

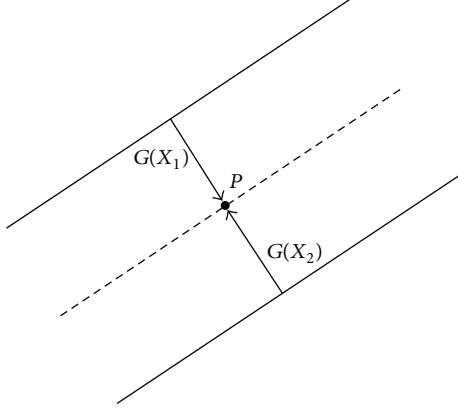


FIGURE 5: An example of radial gradient symmetry transform; we can find that the pixel in the vessel area is generally located between two symmetric gradient vectors.

- (2) For these affected pixels $c(p)$, we compute the vessel accumulation image A by the following equation:

$$A(c(p)) = A(c(p)) + \frac{2 \cdot s(p) - \|c(p) - p\|}{2 \cdot s(p)}. \quad (9)$$

- (3) Then the $VL_G(X)$ is given by

$$VL_G(X) = NL(X) \cdot \left(\frac{A}{M_n}\right)^q, \quad (10)$$

where M_n is a normalization factor and q is a radial strictness parameter.

- (4) For each pixel p , we search in its neighborhood $[p - \Delta p, p + \Delta p]$ along the gradient direction with $\Delta p = 2 \cdot s(p) \cdot g(p)$. As shown in Figure 5, if there exist points X_1 and X_2 that meet the following condition, $\text{Flag}_G(p) = 1$, otherwise; $\text{Flag}_G(p) = 0$:

$$\|G(X_1)\| \geq \|G(p)\|, \quad \|G(X_2)\| \geq \|G(p)\|, \quad (11)$$

$$g(X_1) \approx -g(X_2).$$

- (5) For symmetric vessel likeness function $VL_{\text{Sym}}(X)$, we set a vessel likeness threshold T_h to extract a coarse vasculature. After that, we take an erosion step to get a narrowed retinal vasculature. We then compute the pixel number of connected vessels. If the pixel number is smaller than the preset threshold T_{num} , we consider it as the background noise and it should be removed.

2.4. Graph-Cut Step. Throughout the previous processing steps, we have got a coarsely extracted vasculature. The final step is to accurately segment vessels from previous results. This can be described as a pixel labeling problem which can be formulated using the energy function:

$$E(L) = E_d(L) + kE_s(L), \quad (12)$$

where L is a labeling set and $E_d(L) = \sum_{p \in P} U_p(l_p)$ is the data prior energy, which measures the cost of giving a label $l_p \in L$ to a given pixel p according to prior information. $E_s(L) = \sum_{N \subset P} \sum_{q \in N} V_{pq}(l_p, l_q)$ is the potential energy, which measures the smoothness of a neighboring pixel system N and k is a weighting parameter.

We adopt the graph-cut algorithm to optimize the energy function (12). The centerline is used as shape prior to guide the extraction process. In our framework, a graph $G = (V, \varepsilon)$ is created with nodes corresponding to pixels $p \in P$ of a retinal image, where V is the set of all nodes and ε is the set of all links connecting neighboring nodes. The neighboring pixel system is constructed with eight neighboring pixels. The terminal nodes are defined as source S and sink T . As an initial, we extract the centerline of previously extracted vasculature. The pixels on the centerline are considered as definite foreground F_d and the pixels with $VL_{\text{Sym}}(X) > T_h$ are classified as candidate foreground F_c . The pixels with $VL_{\text{Sym}}(X) < T_l$ are classified as background B_d and others are classified as the candidate background B_c . That is, $L = \{f_d, f_c, b_c, b_d\}$ and $V = \{S, T\} \cup \{F_d, B_d\} \cup \{F_c, B_c\}$.

For each pixel $p \in \{F_c, B_c\}$, we compute its minimum distances to S and T according to the literature [22], which are denoted as $d_f(p)$ and $d_b(p)$, respectively. The cost of t -links can be computed as follows:

$$U_S(p) = \infty, \quad U_T(p) = 0, \quad p \in F_d,$$

$$U_S(p) = 0, \quad U_T(p) = \infty, \quad p \in B_d,$$

$$U_S(p) = \frac{w_1 \cdot VL_{\text{Sym}}(p)}{D_F(p)}, \quad U_T(p) = \frac{w_2 \cdot VL_{\text{Sym}}(p)}{D_F(p)},$$

$$p \in F_c,$$

$$U_S(p) = \frac{w_2 \cdot VL_{\text{Sym}}(p)}{D_F(p)}, \quad U_T(p) = \frac{w_1 \cdot VL_{\text{Sym}}(p)}{D_F(p)},$$

$$p \in B_c, \quad (13)$$

where $D_F(p) = d_f(p)/(d_f(p) + d_b(p))$, $D_B(p) = 1 - D_F(p)$, and $w_1 > 1 > w_2 > 0$. The nodes in F_d and B_d are definitely labeled as f_d and b_d , respectively. The weight of n -link describes the labeling coherence of a pixel with its neighbors. We utilize the pixel value information as the neighborhood penalty item. The cost of n -links can be defined as follows:

$$V_{pq}(l_p, l_q) = \frac{1}{|I(p) - I(q)| + \eta}, \quad (14)$$

where η is a tiny number to avoid division by 0. When the graph-cut algorithm terminates, we encourage candidate foreground pixels to be labeled as foreground and discourage candidate background to be classified as background pixels.

3. Experiments and Conclusion

We test our method on the publicly available databases: DRIVE [5]. Three measures sensitivity (SE), specificity (SP),

TABLE 1: Comparison of different segmentation methods.

STARE	SE (mean/sd.)	SP (mean/sd.)	AC (mean/sd.)
Staal et al. [5]	0.7194/0.0694	0.9773/0.0087	0.9441/0.0065
Mendonça and Campilho [10]	0.7315/NA	0.9781/NA	0.9463/NA
Wang et al. [21]	0.7810/0.0340	0.9770/0.0071	NA
Marín et al. [7]	0.7067/0.0628	0.9801/0.0104	0.9452/0.0064
Ours	0.9074/0.0332	0.9119/0.0320	0.9113/0.0280

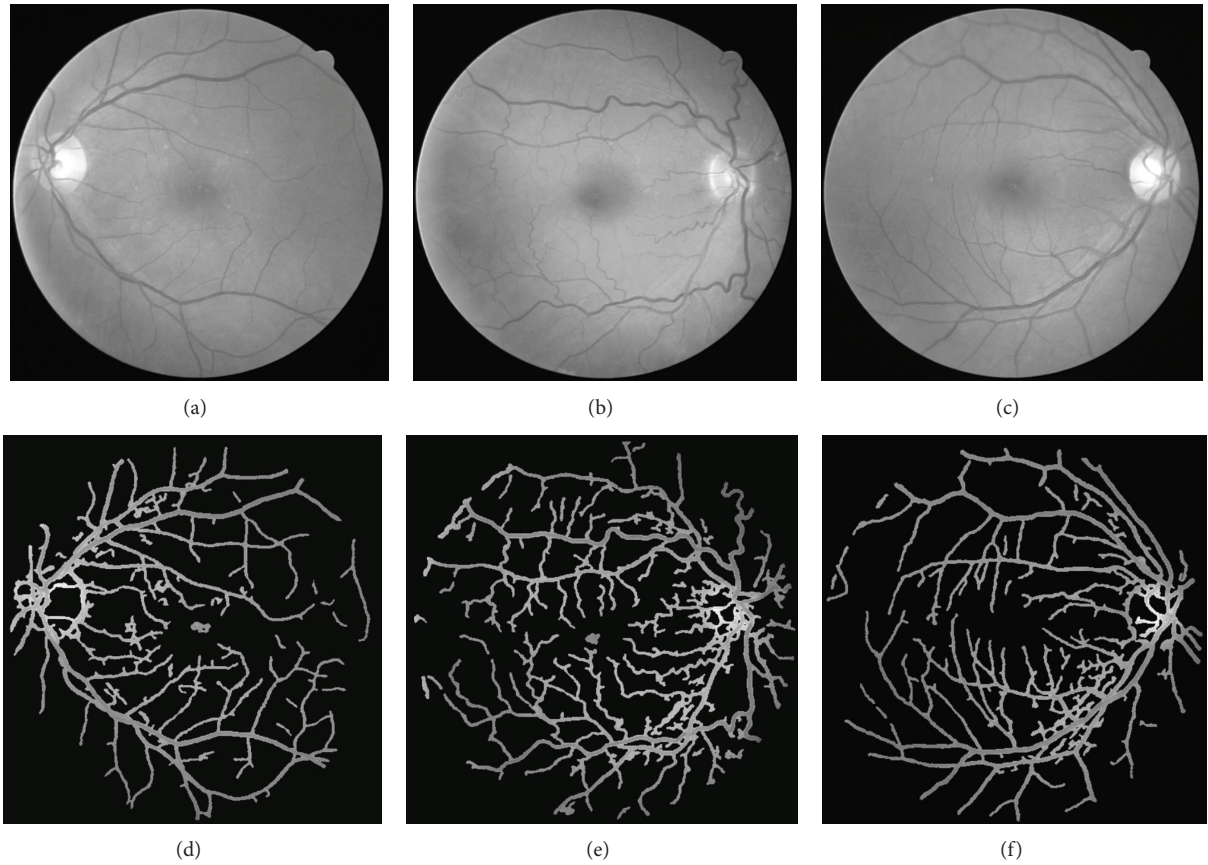


FIGURE 6: An example of 3 extraction results: the first row shows 3 input retinal images and the second row shows the segment results of the retinal vessels.

and accuracy (AC) are used to evaluate the performance of our method in the image field of view. They are defined as follows:

$$\begin{aligned}
 SE &= \frac{N_{\text{correct_vessel}}}{N_{\text{vessel}}}, \\
 SP &= \frac{N_{\text{correct_nonvessel}}}{N_{\text{nonvessel}}}, \\
 AC &= \frac{N_{\text{correct_total}}}{N_{\text{total}}},
 \end{aligned} \tag{15}$$

where $N_{\text{correct_vessel}}$ is the number of correctly classified vessel pixels and N_{vessel} is the number of the vessel pixels in ground truth. $N_{\text{correct_nonvessel}}$ is the number of correctly classified nonvessel pixels and $N_{\text{nonvessel}}$ is the number of nonvessel pixels. $N_{\text{correct_total}}$ is the total number of

correctly classified pixels and N_{total} is total number of pixels.

We test the proposed method on 40 images and compare it with the methods developed by Staal et al. [5], Mendonça and Campilho [10], Wang et al. [21], and Marín et al. [7]. The mean values and standard deviations (sd.) of these methods are shown in Table 1. Some values that cannot be obtained from the literature are denoted by NA.

From Table 1 we can see that there is a prominent improvement in sensitivity. This means that our method is quite effective in extracting some tiny vessels. On the other hand, our method is not as well as others' in both specificity and accuracy. For clinical application, the accuracy should be better than 90%. Our method is over the qualified standard, but there are still large improvements need to be done.

Some of the extraction results are shown in Figures 6 and 7. As it can be seen from Figure 6, the majority of the vessels

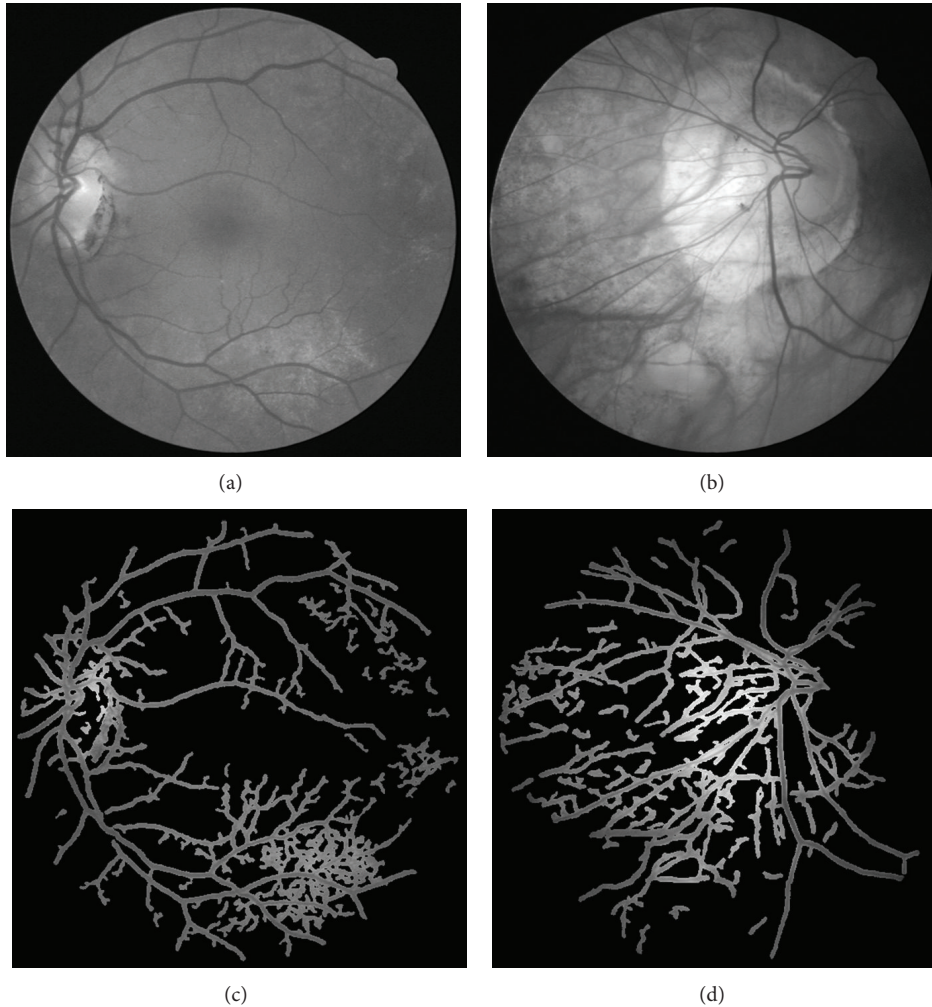


FIGURE 7: Two segmentation results of ill-conditioned retinal images; the speckles greatly reduce the performance of our algorithm.

in the retina can be finely extracted; however, some nonvessel structures are also extracted and some tiny vessels are not correctly segmented. This is mainly because our method focused more on tiny vessel extraction, which is not easy for ophthalmologists to extract manually. Therefore some boundaries between retinal region and the background are mistakenly recognized as vessels. Besides that, the optic disk also cannot be fully excluded from the final result. Figure 7 shows two segmentation results of ill-conditioned retinal images, where some speckles are hard to be differentiated from tiny vessels. Our method fails to extract an accurate vasculature, where the AC values are 0.8720 and 0.8814, respectively. Furthermore, we exchange the order of nonlocal mean filtering and multiscale hessian-based enhancement. Experimental results show that there is a little difference between the performances. This also indicates that nonlocal mean filter is very robust and could be widely used in image processing area.

In summary, this paper first presents a multiscale hessian-based enhancement for retinal images. Next, we adopt an effective nonlocal mean filtering step to suppress noise of the enhanced image. Then, we propose a radial gradient symmetry transform method to suppress the nonvessel artifacts.

Finally, a graph-cut step is taken to accurately segment the retinal vessels. Experiments show that our method is very sensitive for the vessels segmentation, but the performance for some tiny vessel extraction and speckles exclusion is still needed to be improved. This will be our further work. We will make further studies to improve the performance.

Acknowledgments

This work is supported in part by the Natural Science Foundation of Jiangsu Province (Grant no. BK2011331), National Science Foundation of China (Grant no. 61201117), Special Funded Program on National Key Scientific Instruments and Equipment Development (Grant no. 2011YQ040082), and the 2nd Phase Major Project of Suzhou Institute of Biomedical Engineering and Technology (Grant no. Y053011305).

References

- [1] C. Sanchez-Galeana, C. Bowd, E. Z. Blumenthal, P. A. Gokhale, L. M. Zangwill, and R. N. Weinreb, "Using optical imaging summary data to detect glaucoma," *Ophthalmology*, vol. 108, no. 10, pp. 1812–1818, 2001.

- [2] S. Wang, L. Xu, Y. Wang, Y. Wang, and J. B. Jonas, "Retinal vessel diameter in normal and glaucomatous eyes: the Beijing eye study," *Clinical and Experimental Ophthalmology*, vol. 35, no. 9, pp. 800–807, 2007.
- [3] G. Garhöfer, C. Zawinka, H. Resch, P. Kothy, L. Schmetterer, and G. T. Dorner, "Reduced response of retinal vessel diameters to flicker stimulation in patients with diabetes," *British Journal of Ophthalmology*, vol. 88, no. 7, pp. 887–891, 2004.
- [4] H. Yatsuya, A. R. Folsom, T. Y. Wong, R. Klein, B. E. K. Klein, and A. R. Sharrett, "Retinal microvascular abnormalities and risk of lacunar stroke: Atherosclerosis Risk in Communities Study," *Stroke*, vol. 41, no. 7, pp. 1349–1355, 2010.
- [5] J. Staal, M. Abramoff, M. Niemeijer, M. A. Viergever, and B. van Ginneken, "Ridge-based vessel segmentation in color images of the retina," *IEEE Transactions on Medical Imaging*, vol. 23, no. 4, pp. 501–509, 2004.
- [6] J. V. B. Soares, J. J. G. Leandro, R. M. Cesar Jr., H. F. Jelinek, and M. J. Cree, "Retinal vessel segmentation using the 2-D Gabor wavelet and supervised classification," *IEEE Transactions on Medical Imaging*, vol. 25, no. 9, pp. 1214–1222, 2006.
- [7] D. Marín, A. Aquino, M. E. Gegúndez-Arias, and J. M. Bravo, "A new supervised method for blood vessel segmentation in retinal images by using gray-level and moment invariants-based features," *IEEE Transactions on Medical Imaging*, vol. 30, no. 1, pp. 146–158, 2011.
- [8] M. Sofka and C. V. Stewart, "Retinal vessel centerline extraction using multiscale matched filters, confidence and edge measures," *IEEE Transactions on Medical Imaging*, vol. 25, no. 12, pp. 1531–1546, 2006.
- [9] B. S. Y. Lam, Y. Gao, and A. W. C. Liew, "General retinal vessel segmentation using regularization-based multiconcavity modeling," *IEEE Transactions on Medical Imaging*, vol. 29, no. 7, pp. 1369–1381, 2010.
- [10] A. M. Mendonça and A. Campilho, "Segmentation of retinal blood vessels by combining the detection of centerlines and morphological reconstruction," *IEEE Transactions on Medical Imaging*, vol. 25, no. 9, pp. 1200–1213, 2006.
- [11] Y. Boykov, O. Veksler, and R. Zabih, "Fast approximate energy minimization via graph cuts," *IEEE Transactions on Pattern Analysis and Machine Intelligence*, vol. 23, no. 11, pp. 1222–1239, 2001.
- [12] Y. Boykov and V. Kolmogorov, "An experimental comparison of mincut/max-flow algorithms for energy minimization in vision," *IEEE Transactions on Pattern Analysis and Machine Intelligence*, vol. 26, no. 9, pp. 1124–1137, 2004.
- [13] Y. Boykov and G. Funka-Lea, "Graph cuts and efficient N-D image segmentation," *International Journal of Computer Vision*, vol. 70, no. 2, pp. 109–131, 2006.
- [14] X. Chen, J. K. Udupa, U. Bagci, Y. Zhuge, and J. Yao, "Medical image segmentation by combining graph cuts and oriented active appearance models," *IEEE Transactions on Image Processing*, vol. 21, no. 4, pp. 2035–2046, 2012.
- [15] D. Freedman and T. Zhang, "Interactive graph cut based segmentation with shape priors," in *Proceedings of the IEEE Computer Society Conference on Computer Vision and Pattern Recognition (CVPR '05)*, pp. 755–762, June 2005.
- [16] X. Chen, M. Niemeijer, L. Zhang, K. Lee, M. D. Abramoff, and M. Sonka, "Three-dimensional segmentation of fluid-associated abnormalities in retinal OCT: probability constrained graph-search-graph-cut," *IEEE Transaction on Medical Imaging*, vol. 31, no. 8, pp. 1521–1531, 2012.
- [17] D. Xiang, J. Tian, K. Deng, X. Zhang, F. Yang, and X. Wan, "Retinal vessel extraction by combining radial symmetry transform and iterated graph cuts," in *Proceedings of the Annual International Conference of the IEEE Engineering in Medicine and Biology Society*, pp. 3950–3953, 2011.
- [18] A. F. Frangi, W. J. Niessen, K. L. Vincken, and M. A. Viergever, "Multiscale vessel enhancement filtering," in *Medical Imaging Computing and Computer Assisted Interventions*, vol. 1496 of *Lecture Notes in Computer Sciences*, pp. 130–137, 1998.
- [19] A. Buades, B. Coll, and J. M. Morel, "A non-local algorithm for image denoising," in *Proceedings of the IEEE Computer Society Conference on Computer Vision and Pattern Recognition (CVPR '05)*, pp. 60–65, June 2005.
- [20] G. Loy and A. Zelinsky, "Fast radial symmetry for detecting points of interest," *IEEE Transactions on Pattern Analysis and Machine Intelligence*, vol. 25, no. 8, pp. 959–973, 2003.
- [21] L. Wang, A. Bhalerao, and R. Wilson, "Analysis of retinal vasculature using a multiresolution hermite model," *IEEE Transactions on Medical Imaging*, vol. 26, no. 2, pp. 137–152, 2007.
- [22] Y. Li, J. Sun, C. Tang, and H.-Y. Shum, "Lazy snapping," *ACM Transactions on Graphics*, vol. 23, no. 3, pp. 303–308, 2004.

Research Article

A New Multichannel Spectral Imaging Laser Scanning Confocal Microscope

Yunhai Zhang, Bian Hu, Yakang Dai, Haomin Yang, Wei Huang, Xiaojun Xue, Fazhi Li, Xin Zhang, Chenyu Jiang, Fei Gao, and Jian Chang

Suzhou Institute of Biomedical Engineering and Technology, Chinese Academy of Sciences, Suzhou 215163, China

Correspondence should be addressed to Yakang Dai; daiyk@sibet.ac.cn

Received 3 January 2013; Accepted 24 February 2013

Academic Editor: Jimin Liang

Copyright © 2013 Yunhai Zhang et al. This is an open access article distributed under the Creative Commons Attribution License, which permits unrestricted use, distribution, and reproduction in any medium, provided the original work is properly cited.

We have developed a new multichannel spectral imaging laser scanning confocal microscope for effective detection of multiple fluorescent labeling in the research of biological tissues. In this paper, the design and key technologies of the system are introduced. Representative results on confocal imaging, 3-dimensional sectioning imaging, and spectral imaging are demonstrated. The results indicated that the system is applicable to multiple fluorescent labeling in biological experiments.

1. Introduction

As an effective and necessary scientific instrument for observing small structures, laser scanning confocal microscopy has been widely applied in tissue biology, cell biology, molecular biology, genomics, embryology, neurology, embryology, pathology, immunology, epidemiology, oncology, bacteriology and virology, and so forth [1–4]. The confocal system uses the spatial filter techniques to eliminate the out-of-focal-plane light. Only the light from the focal plane can be detected. Hence, the system has high spatial resolution and signal-to-noise ratio [5]. At the same time, it has the capability of optical sectioning in z axis direction, which enables 3-dimensional imaging of thick samples [6].

The confocal concept was proposed by Minsky in 1950s [7]. The first commercial product was released in 1987. After that, the confocal techniques have attracted researchers' attention, and new developments in both research and products were achieved. To date, various aspects of the system have been investigated to improve the image resolution [8, 9], and products with new functions have been launched in the market.

Currently, there is a need to image multiple fluorescent labeling tissues simultaneously, discriminate the various fluorescent components [10], and implement complex functional experiments, such as fluorescence recovery after

photobleaching (FRAP) [11], fluorescence resonance energy transfer (FRET) [12], and fluorescence lifetime imaging microscopy (FLIM) [13]. We thus developed a new multichannel spectral imaging laser scanning confocal microscope to meet these demands. The following sections describe the methodology of the system and demonstrate representative experimental results on the system.

2. System Design

The hardware of multi-channel spectral imaging laser scanning confocal microscope consists of a fluorescence microscope, a confocal scanning head, a laser source, an electrical control box, and a computer. Modular design is used in the system; the confocal scanning and multi-channel spectral imaging are integrated into the scanning head; the multiple lasers are placed in a laser cabinet; the scanning head and laser cabinet are separated to avoid laser vibration effects on the confocal imaging; the complex electrical control parts are integrated into an electrical control box; the control software is installed in the computer.

The fluorescence microscope has an independent illumination system (high-pressure mercury lamp for epillumination and tungsten halogen lamp for transmission illumination) and an optical path for visual observation.

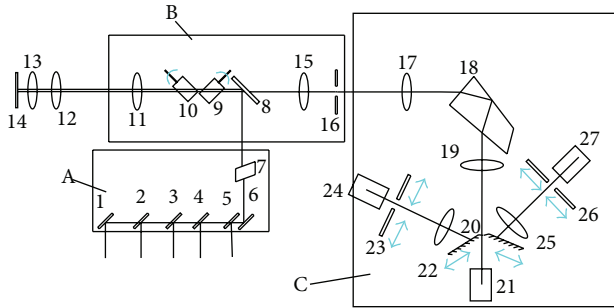


FIGURE 1: Diagram of the confocal scanning head. A: Laser combination and selection module, B: confocal scanning imaging module, C: multi-channel spectral imaging module, 1: dichroic mirror for spare laser combination, 2–5: dichroic mirror for four lasers combination, 6: mirror, 7: acousto-optical tunable filter (AOTF), 8: dichroic mirror for excitation and fluorescence separation, 9–10: X-Y galvanometer optical scanner, 11: scanning lens, 12: tube lens, 13: objective lens, 14: sample slide, 15: pinhole lens, 16: pinhole, 17: collimation lens, 18: prism, 19: focal lens, 20: movable slit 1, 21, 24, 27: PMTs, 22, 25: relay lens, 23, 26: movable slit 2, 3.

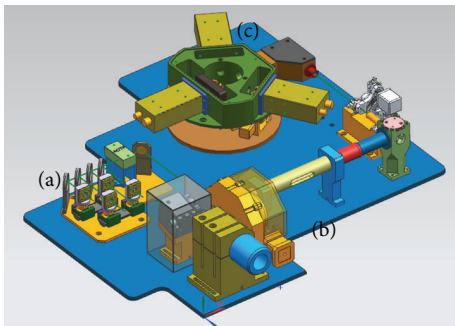


FIGURE 2: Internal composition of the confocal scanning head.

The optical path for visual observation is used for initial observation and localization of the sample before switching to the confocal system. The confocal system also has an independent illumination system (multiple lasers) and a detection system (PMTs). The 2-dimensional optical sectioning, 3-dimensional imaging, and selected spectral bandwidth imaging can be implemented through control software.

Figure 1 is the diagram of the confocal scanning head, which is the key component of the confocal microscopy. The internal composition is shown in Figure 2. It can be divided into three parts: (a) laser combination and selection module, (b) confocal scanning imaging module, and (c) multi-channel spectral imaging module.

In the laser combination and selection module, the four fiber-coupled semiconductor lasers (405 nm, 488 nm, 561 nm, and 638 nm) are combined into one beam using dichroic mirrors, then the combined beam goes through the AOTF. The combined beam's laser wavelength and power can be adjusted by changing the frequency and amplitude of the ultrasonic wave. The spare space is reserved for the additional laser extension for the future upgrade.

The confocal scanning imaging module is mainly composed of scanning lens, X-Y galvanometer optical scanner, dichroic mirror dial, pinhole lens, and three aperture-variable pinholes. The laser is reflected from the dichroic mirror assembly and steered by the X-Y galvanometer optical scanner. Then, it goes through the scanning lens and is focused on the sample by the objective lens. The excited fluorescence is recollected by the same objective lens, goes through the scanning lens and dichroic mirror assembly, and is focused at pinhole by the pinhole lens. There is an individual dichroic mirror assembly (including a dichroic mirror and a fluorescence filter) for each laser wavelength. For the multiple lasers, there is another dichroic mirror assembly. An aperture-variable pinhole is for 60x oil immersion objective lens. The second one is for 100x oil immersion objective lens. The third one is used to balance image resolution and signal-to-noise ratio.

The multi-channel spectral imaging module is based on light separation of the prism. There are three spectral detection channels. The spectrum of the fluorescence is expanded by the prism's dispersion. At the focal plane of the fluorescence, there are two movable mirrors. Part or all of the fluorescence passes through the slit between the two mirrors and is collected by the first spectral channel. The fluorescence can also be reflected by the two movable mirrors and then goes to the second and third spectral detection channels individually. There are two movable diaphragms in the second and third spectral channels, which can be used to control the spectral band width of the fluorescence by adjusting the location and the size.

3. Key Technologies

The multi-channel spectral imaging laser scanning confocal microscopy involves several key technologies, such as high-speed synchronization control of galvanometer scanning, 3-dimensional optical sectioning imaging, multi-channel spectral imaging, spatial fine pinhole filter technique [4], and optimization of the point spread function for illumination [8]. The first three are the foundation of the confocal microscopy and will be discussed in the follow paragraphs.

3.1. High-Speed Synchronization Control of Galvanometer Scanning. The scanning control system is responsible for the control signal generation for the galvanometer. The data acquisition and hardware synchronization are realized by the combination of sampling signal control system and galvanometer scanning control system. It ensures the accuracy of scanning data for the image reconstruction. Figure 3 is the diagram of the galvanometer synchronization control system. ARM accomplishes the function of user interface, calculation of waveform data, parameters' setup for sampling signal, and writing operation to FPGA. FPGA module realizes the function of DDS signal generation and sampling control signal generation. DAC transforms the output of the FPGA to the analog voltage signal, which is used to control the movement of the galvanometer scanner.

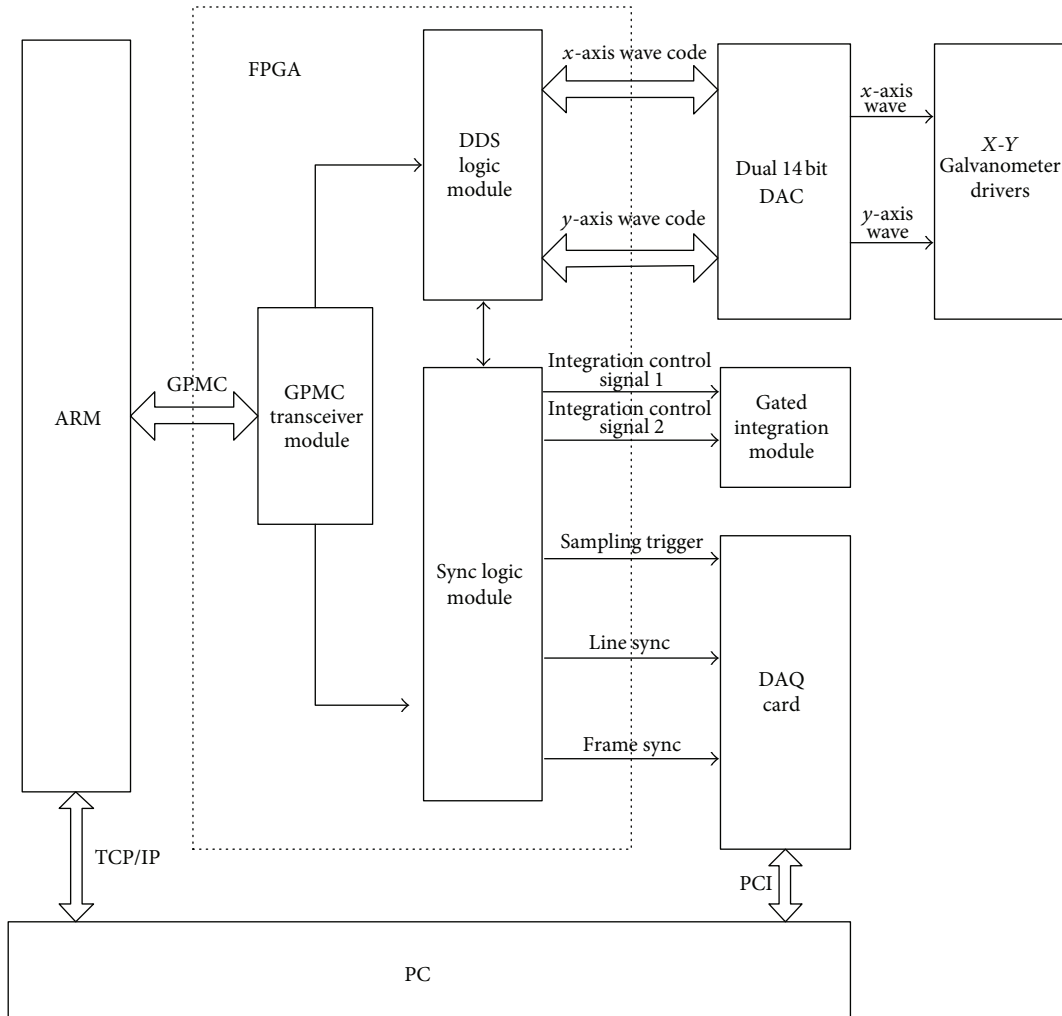


FIGURE 3: Diagram of the galvanometer synchronization control system.

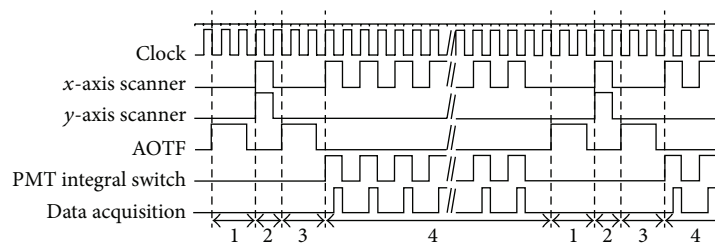


FIGURE 4: Synchronization between the galvanometer scanner control and data acquisition. Phase 1: AOTF is switched off after one line scanning, phase 2: x-axis and y-axis scanners retrace to the start position for the next line scanning, phase 3: AOTF is switched on, phase 4: process of one line scanning.

The strict synchronization between the galvanometer scanner and data acquisition is very important. In the fast retracing scanning process, data is not collected. To avoid the photobleaching of fluorescence, AOTF is used for rapid switch off of laser [14]. The synchronization between the galvanometer scanner control and data acquisition is shown in Figure 4. The requirement for the synchronization is as follows: (i) frame synchronization signal (the rising edge of the

square wave). It has the same frequency as the slow scanning trigger signal. It appears on the rising edge of the square wave during the slow scanning process. (ii) Line synchronization signal. The data is collected whenever the trigger voltage is at the high level. The whole line data are obtained at each high level trigger signal. It has the same frequency as the fast scanning trigger signal. The trigger signal is at high level when it is in scanning, while it is at low level when it is in the

retracing process. (iii) Sampling pulse. The sampling pulse is generated when the line synchronization signal is high. The sampling control signal is synchronized with galvanometer control voltage from the DAC.

3.2. 3-Dimensional Optical Sectioning Imaging. One feature of the confocal microscopic imaging is that only the very thin tissue in the focal plane can be imaged once a time. The tissue above or below the focal plane cannot be imaged due to the block of the pinhole. This feature makes the confocal microscopic imaging suitable for the lossless sectioning imaging. After collecting a series of 2-dimensional images, 3-dimensional image of the tissue can be reconstructed.

During the experiment, the sample tissue needs to be moved accurately in the z direction with the step size of $0.2\ \mu\text{m}$. A piezo nanopositioner meets the requirement. The parameters such as single step size and total step numbers can be adjusted by the control software. Those parameters are the basis of the 3-dimensional confocal images. Figure 5 demonstrates the control program of nanopositioner using LabVIEW. Firstly, the positioner is initialized according to the setting of start position, end position, and number of slices. Then, the positioner is moved to the start position, and the movement of each slice is calculated. It is kept in the current position during the process of 2-dimensional scanning. After that, it is moved to the next slice and a new 2-dimensional scanning starts. The process is sequentially cycled until finishing the number of slices. During the process, the interface shows the actual position of the nanopositioners.

In order to get a series of 2-dimensional confocal images, a relatively long time is needed. During the time, the sample slide should be fixed, which requires that the supporting structure for the slide and microscope base have enough rigidity. However, it is still hard to eliminate all the small drifts during the long data acquisition time. So, postprocessing algorithms such as image registration are needed to correct the drifts.

The 3-dimensional image is reconstructed from a series of 2-dimensional images using volume rendering. The volume rendering method resamples the collected 3-dimensional data and transforms the data into 2-dimensional discrete signals in image display cache. It classifies the 3-dimensional data, sets color and opacity for each voxel, and generates the 2-dimensional display image according to the illumination and shading model. Main algorithms of volume rendering include ray casting, footprint tracing, and shear deformation. The ray casting is used in our system.

3.3. Multichannel Spectral Imaging. In the case that multiple fluorescence is excited simultaneously, single channel or multi-channel detection is needed to effectively differentiate the fluorescence components. Fluorescence efficiency, spectral resolution, dispersion linearity, and stray light effect need to be considered in the design.

The fluorescence usually is weak for biological samples. So, the light transmission efficiency is very important for the design of the fluorescence spectrometer. In the visible

spectrum, the maximum efficiency of the grating spectrometer is only $1/2\text{--}2/3$ of that of prism spectrometer. The efficiency decreases to $1/4$ of that of prism spectrometer when it is far away from the blazed wavelength. Hence, grating spectrometer loses more fluorescence for the weak signal detection.

In the confocal system, the grating area used is very small and the line number is at the level of 10^3 . The theoretical resolution is higher than prism. However, the required minimum spectral band width is only 5 nm. The high spectral resolution of the grating spectrometer is not fully utilized.

Compared with linear dispersion of grating spectrometer, dispersion of prism spectrometer is nonlinear. In the confocal system, the user needs to select the spectral band before data acquisition. So the nonlinear dispersion has little effect on the imaging system.

Stray light of prism spectrometer mainly comes from prism surface reflection. After antireflection coating on the prism surface, stray light decreases to 10^{-3} or less. For the grating spectrometer, stray light comes from many sources such as grating diffraction energy level overlap, 30–40% unused energy from zero order, and high orders. The non-working surface of the grating groove and ghost lines caused by grating ruling error also contributes to the generation of stray light.

So, the prism spectrometer outperforms the grating spectrometer and is thus used in the system.

Due to the cost limitation, there are 3 fluorescence detection channels in the system. It can be extended to have more channels as desired. The multi-channel spectral imaging system based on prism is shown in Figure 1. The spectral range of detection of each channel can be adjusted from 400 to 700 nm. The minimum spectral band width is 5 nm and the maximum band width is 300 nm.

In the system, constant deviation angle is used to expand the spectrum. The optical path is rotated 90 degrees to make sure that the total deviation angle is constant after the prism for the light in the minimum deviation condition. The dispersion function of constant deviation angle of the prism is equal to the prism with the apex angle of 60 degrees.

The fluorescence from the sample is focused on the image plane after collimation. The prism is fixed, and the detected central wavelength and spectral band width can be adjusted by the exit slit assembly. In Figure 1, the exit slit 1 is located at the focal plane. The two blades of the slit, coated with reflective film, are tilted to both sides by 30 degrees independently. The light reflected from the blades' surface goes to the channel 2 and 3. Slit 1 controls the spectral band width detected in PMT 1. Slit 2 and 3 adjust the spectral band width detected in PMT 2 and 3 separately.

4. Experiment Results

Figure 6 shows the system setup. (a) is the laser source, (b) is the X-Y galvanometer optical scanner, (c) is the nanopositioner, and (d) is the detector. In the system, oil immersion objective UPLSAPO 100x from Olympus was used. The NA is 1.4 and working distance is 0.13 mm. Super

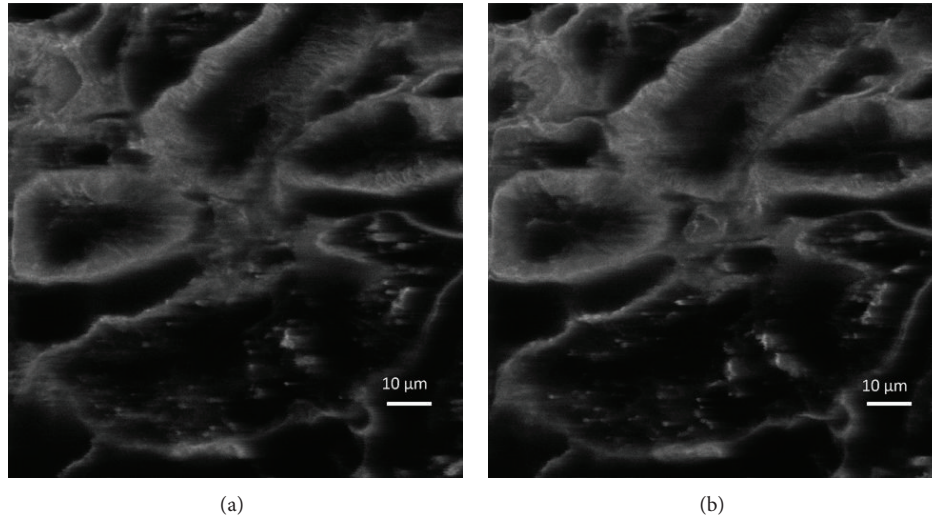


FIGURE 8: Two confocal images at various depths.

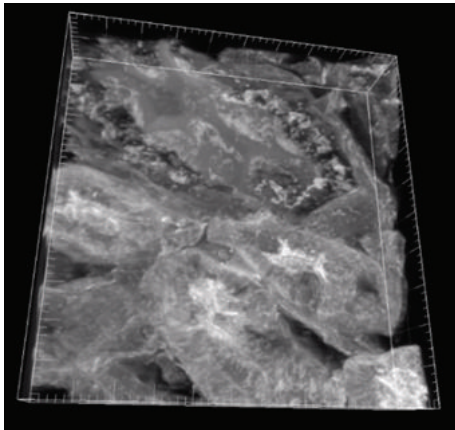


FIGURE 9: Reconstructed 3-dimensional image.

100 images. They are shown in Figures 8 and 9. The two images of Figure 8 were focused on the two different depths in z position. The distance between the two images was $1.2 \mu\text{m}$. It can be observed that the details of the tissue were changed.

4.3. Confocal Spectral Imaging Experiment. An improved spectrometer was added before the detector and the incident slit were removed. The pinhole was imaged at incident slit and a circular slit was formed. The exit slit was replaced by a slit with adjustable position and width. The spectrum of fluorescent dye Cy5 excited by 638 nm laser is shown in Figure 10(a). The bandwidth of the spectrum was 50 nm. The fluorescence in particular bandwidth can be imaged by changing the position and bandwidth of the slit. By the calculation, the $50 \mu\text{m}$ slit corresponded to 2.5 nm spectrum bandwidth. It is shown in Figure 10(b).

In the experiment, the illumination source was 405 nm laser. The biological tissue was rat kidney sliced from Molecular Probes. In the slice, the nuclei were counterstained

with the blue-fluorescent DNA stain DAPI. Image area was $106 \mu\text{m} \times 110 \mu\text{m}$. The full spectrum image and image with 2.5 nm bandwidth are shown in Figure 11. In both images, the nuclei were clearly observed. The fluorescent light became weak and signal-to-noise ratio became worse when the spectrum bandwidth decreased.

The system has the advantage of illumination of multiple fluorescent components simultaneously and confocal imaging of multiple detection channels. Each channel can be used for spectral imaging and spectral analysis. Prism was applied to split the spectrum, which has higher light utilization efficiency, compared to grating method. This is very important for the weak fluorescence signal. In addition, the stray light of the prism is relatively small. So the image can be obtained at higher signal-to-noise ratio. Due to the realization of multi-channel simultaneously spectral imaging, the disadvantage of the system is that many parts need to be controlled simultaneous. Hence, the control system is very complex and requires the synchronization of all parts. Besides, the real-time display of images requires intensive computation of image reconstruction and processing. The graphic workstation with high performance is needed.

5. Conclusions

This paper introduces our newly developed multi-channel spectral imaging laser scanning confocal microscope. The system design and key technologies (such as high-speed synchronization, control of galvanometer scanning, 3-dimensional optical sectioning imaging, and multi-channel spectral imaging) are described. The experimental results demonstrate that the system is capable of multifluorescent spectral imaging. Our multi-channel spectral imaging laser scanning confocal microscope has many advantages. Firstly, it can excite multiple dyes simultaneously and differentiate various fluorescent components effectively. In the system, four lasers of 405 nm, 488 nm, 561 nm, and 638 nm were



FIGURE 10: Spectrum energy distribution for Cy5.

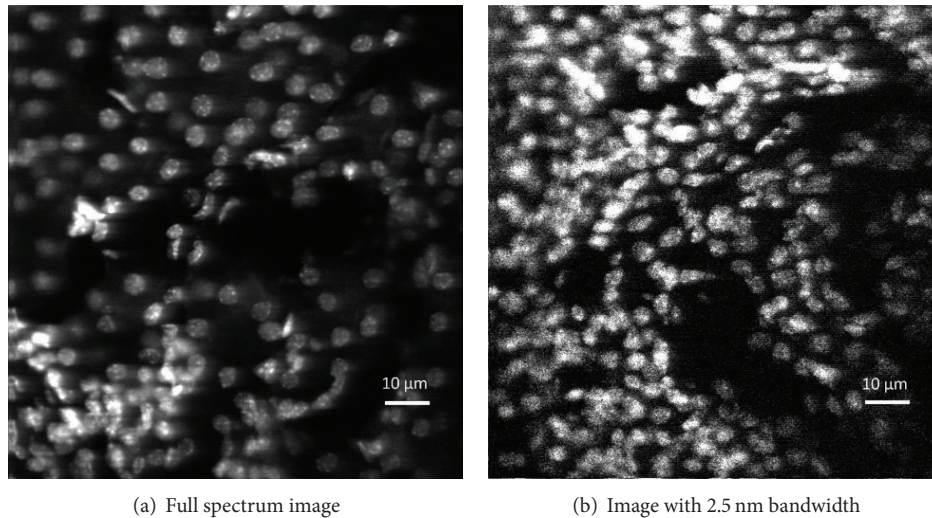


FIGURE 11: Confocal images for dye DAPI in rat kidney with various bandwidth.

used as illumination source. The laser source module is scalable. Additional laser extension is available for the user's upgrade. Secondly, the different spectral components from the same dye can be imaged and postprocessed to meet the requirements of biological experiments. Three fluorescence detection channels realized multiple spectral imaging simultaneously. The detected spectrum's central wavelength and spectral width can be adjusted individually for each channel. The information from the detected spectrum is fully utilized. Thirdly, the illumination and shading model was improved, and 3-dimensional image reconstruction algorithm was optimized especially for confocal sectioning images. The image reconstruction time was greatly decreased from 30 seconds to 15 seconds.

Acknowledgments

This work was supported in part by the SIBET Projects Y052031205 and Y053011305, NSFC Grant 61201117, and NSFJ Grant BK2011331.

References

- [1] "Cell Biological Applications of Confocal Microscopy," in *Methods in Cell Biology*, B. Matsumoto, Ed., vol. 70, Academic Press, New York, NY, USA, 2002.
- [2] A. R. Hibbs, *Confocal Microscopy for Biologists*, Kluwer Academic Publishers, New York, NY, USA, 2004.
- [3] E. J. G. Peterman, H. Sosa, and W. E. Moerner, "Single-molecule fluorescence spectroscopy and microscopy of biomolecular motors," *Annual Review of Physical Chemistry*, vol. 55, pp. 79–96, 2004.
- [4] J. L. Dobbs, H. Ding, A. Benveniste et al., "Confocal fluorescence microscopy for evaluation of breast cancer in human breast tissue," in *Proceedings of the Biomedical Optics*, paper BTu3A. 19, OSA Technical Digest, Optical Society of America, Miami, Fla, USA, 2012.
- [5] J. J. Hunter, C. J. Cookson, M. L. Kislak, J. M. Bueno, and M. C. W. Campbell, "Characterizing image quality in a scanning laser ophthalmoscope with differing pinholes and induced scattered light," *Journal of the Optical Society of America A*, vol. 24, no. 5, pp. 1284–1295, 2007.
- [6] R. Uhl, R. Daum, H. Harz, C. Seebacher, and S. Neogy, "High throughput high content live cell screening platform," in *Biophotonics 2007: Optics in Life Science*, J. Popp and G. von Bally, Eds., vol. 6633 of *Proceedings of the SPIE*, Munich, Germany, 2007.
- [7] M. Minsky, "Microscopy Apparatus," US patent 3,013,467, 1961.
- [8] B. R. Boruah, "Lateral resolution enhancement in confocal microscopy by vectorial aperture engineering," *Applied Optics*, vol. 49, no. 4, pp. 701–707, 2010.
- [9] J. Bückers, D. Wildanger, G. Vicidomini, L. Kastrup, and S. W. Hell, "Simultaneous multi-lifetime multi-color STED imaging for colocalization analyses," *Optics Express*, vol. 19, no. 4, pp. 3130–3143, 2011.
- [10] M. B. Sinclair, D. M. Haaland, J. A. Timlin, and H. D. T. Jones, "Hyperspectral confocal microscope," *Applied Optics*, vol. 45, no. 24, pp. 6283–6291, 2006.
- [11] D. Mazza, F. Cella, G. Vicidomini, S. Krol, and A. Diaspro, "Role of three-dimensional bleach distribution in confocal

- and two-photon fluorescence recovery after photobleaching experiments,” *Applied Optics*, vol. 46, no. 30, pp. 7401–7411, 2007.
- [12] S. H. Kim, D. S. Choi, and D. Kim, “Single-molecule detection of fluorescence resonance energy transfer using confocal microscopy,” *Journal of the Optical Society of Korea*, vol. 12, no. 2, pp. 107–111, 2008.
- [13] E. Auksorius, B. R. Boruah, C. Dunsby et al., “Stimulated emission depletion microscopy with a supercontinuum source and fluorescence lifetime imaging,” *Optics Letters*, vol. 33, no. 2, pp. 113–115, 2008.
- [14] D. R. Suhre and N. Gupta, “Acousto-optic tunable filter sidelobe analysis and reduction with telecentric confocal optics,” *Applied Optics*, vol. 44, no. 27, pp. 5797–5801, 2005.

Research Article

Hybrid Multilevel Sparse Reconstruction for a Whole Domain Bioluminescence Tomography Using Adaptive Finite Element

Jingjing Yu,¹ Xiaowei He,² Guohua Geng,² Fang Liu,^{3,4} and L. C. Jiao⁴

¹ School of Physics and Information Technology, Shaanxi Normal University, Xi'an, Shanxi 710062, China

² School of Information Sciences and Technology, Northwest University, Xi'an, Shanxi 710069, China

³ School of Computer Science and Technology, Xidian University, Xi'an, Shanxi 710071, China

⁴ Key Laboratory of Intelligent Perception and Image Understanding of Ministry of Education of China, Xi'an, Shanxi 710071, China

Correspondence should be addressed to Xiaowei He; hexw@nwu.edu.cn

Received 15 September 2012; Accepted 26 January 2013

Academic Editor: Chenghu Qin

Copyright © 2013 Jingjing Yu et al. This is an open access article distributed under the Creative Commons Attribution License, which permits unrestricted use, distribution, and reproduction in any medium, provided the original work is properly cited.

Quantitative reconstruction of bioluminescent sources from boundary measurements is a challenging ill-posed inverse problem owing to the high degree of absorption and scattering of light through tissue. We present a hybrid multilevel reconstruction scheme by combining the ability of sparse regularization with the advantage of adaptive finite element method. In view of the characteristics of different discretization levels, two different inversion algorithms are employed on the initial coarse mesh and the succeeding ones to strike a balance between stability and efficiency. Numerical experiment results with a digital mouse model demonstrate that the proposed scheme can accurately localize and quantify source distribution while maintaining reconstruction stability and computational economy. The effectiveness of this hybrid reconstruction scheme is further confirmed with *in vivo* experiments.

1. Introduction

Bioluminescence imaging (BLI) is an *in vivo* imaging modality that has been successfully used in preclinical researches [1–3]. This imaging strategy exploits the properties of luciferase that can generate visible or near infrared light through the oxidation of an enzyme-specific substrate in the presence of oxygen and adenosine triphosphate [4]. As the produced light intensity is directly proportional to the concentration of luciferase-expressing cells, BLI can reveal cellular and molecular features of biology and disease [5]. However, BLI fails to provide depth information of the internal biological sources [6]. Collecting measurement data from multiple views or combining multiple BLI acquisition with geometrical structures acquired by micro-CT or MRI, bioluminescence tomography (BLT) tries to reconstruct the 3D biological source distribution. In this way, BLT overcomes the limitation of planar imaging in poor spatial resolution and further facilitates our understanding of biomolecular processes as they occur in living animals. Therefore, BLT has

substantial potential to be a powerful tool for noninvasively monitoring and tracking a variety of biological processes [7].

Generally, BLT involves a forward and an inverse problem (source reconstruction). Due to the diffusive nature of photon propagation in tissue, BLT source reconstruction is known to be a highly ill-posed problem [6, 8]. To overcome the inherent ill-posedness of the tomographic problem in BLT, different strategies have been proposed either by increasing the amount of independent measurements with spectrally resolved or multispectral approaches [9–13] or by reducing the number of unknowns with permissible source region [6, 10, 13, 14]. Up to now, quantitative reconstruction for whole domain BLT with monochromatic boundary measurements has not been intensively investigated.

As in many other imaging modalities, the achievable resolution for BLT is determined firstly by the signal to noise ratio, and secondly by the level of discretization. Image quality can be improved by uniformly refining mesh throughout the reconstruction domain. Nevertheless, global refinement tends to further aggravate the ill-posedness and

incur insurmountable computational burden due to the increased unknowns and problem size. Consequently, the use of adaptive finite element method (AFEM) is an indispensable approach to improve image quality [15–21].

In this contribution, we present a whole domain BLT method based on AFEM which provides fine resolution around targets with coarser resolution in other regions. Unlike the previous AFEM-based BLT that adopted identical inversion strategy on different mesh levels [15, 18–21], we take the variance on different discretization levels into account and propose a novel hybrid multilevel reconstruction scheme to maintain solution stability and computational economy. Two different inversion algorithms, the stagewise fast LASSO (SwF-LASSO) [22] and the incomplete variables truncated conjugate gradient method (IVTCG) [23], are applied to the first mesh level and the succeeding ones according to their respective characteristics.

The following sections describe some of the implementation details of the hybrid AFEM algorithm, the evaluations on a digital mouse model, and the validation with an *in vivo* experiment. Short discussions and concluding remarks are given at the end of this paper.

2. Methodology

2.1. Photon Propagation Model. In this work, we assume that the structural and optical parameters regarding different organs are given. Therefore, the BLT reconstruction comes down to a linear inverse source problem. Based on the diffusion approximation model of radiative transfer equation, a linear relationship between the source distribution and boundary measurements is then derived with the finite element method [6]:

$$AS = \Phi^m, \quad (1)$$

where $A \in R^{M \times N}$ ($M < N$) is the system matrix, $S \in R^N$ denotes the internal source distribution, and $\Phi^m \in R^M$ represents measurable boundary nodal photon density that is usually calculated from the surface flux image captured by a CCD camera.

In view of the limitation of using permissible source region in BLT reconstruction, we consider a whole domain reconstruction scheme without this kind of *a priori* information. On the other hand, l_1 -norm based sparse regularization methods have attracted considerable amount of attention in BLT [10, 20–25], and the reconstructions' results therein demonstrate that l_1 -norm solution fits the sparsity nature of bioluminescent source distribution in BLT practice. Using l_1 regularization, we formulate the BLT inverse problem to the following optimization problem:

$$\min \frac{1}{2} \|AS - \Phi^m\|_2^2 + \tau \|S\|_1, \quad (2)$$

where $\|\cdot\|_2$ denotes the Euclidean norm, $\|\cdot\|_1$ is the l_1 norm, and $\tau > 0$ is a regularization parameter.

2.2. Hybrid Multilevel Reconstruction Based on AFEM. In order to provide the resolution necessary for imaging at

acceptable computational cost, the domain Ω is dynamically discretized into a nested sequence of tetrahedral meshes $\{\Theta_1, \dots, \Theta_k, \dots\}$, rather than a fixed and uniformly fine mesh. In the proposed hybrid multilevel AFEM reconstruction process, reconstruction starts at the coarsest level and proceeds to the finer ones by locally refining the particular region based on a previous reconstruction procedure.

We note that the first reconstructed procedure on the coarsest mesh is quite different from the subsequent ones in the following three aspects. (i) It is based on a uniform mesh while others are with a locally refined mesh. (ii) The inversion on the first discretization level involves a large-size underdetermined system. In contrast, all of the subsequent reconstructions on locally finer region involve overdetermined systems. (iii) It has no *a priori* information of a promising region in whole domain case, whereas the others can obtain a permissible source region to constrain the solution space from a previous reconstruction procedure. Consequently, the specific inversion should be different on different meshes, and thus we propose a hybrid multilevel reconstruction scheme.

On the first mesh Θ_1 , we employed the recently reported greedy algorithm SwF-LASSO to solve the underdetermined problem in (2). The SwF-LASSO algorithm converges very fast and is able to find an approximate value close to the real distribution in only a few iteration steps. A brief outline of SwF-LASSO is given as follows [22].

Step 0. Initialization. $n = 0$, index set $O = \{1, 2, \dots, N\}$, $P = \Phi$.

Step 1. Selecting basis function.

For $i \in O$, compute $\Delta L_i^{n+1} = -(q_i^n)^2 / a_i^T a_i$, compute the stagewise threshold $\gamma = \sqrt{\sum_{i \in O} (\Delta L_i^{n+1})^2 / |O|}$ and then determine the index set of the basis functions to be selected $K^{n+1} = \{i : \Delta_0 > |\Delta L_i^{n+1}| > c \cdot \gamma, i \in O\}$.

Step 2. The algorithm will be terminated when the index set $O = \Phi$ is empty, or $|\max_{i \in K^{n+1}} \Delta L_i^{n+1}| < \epsilon$, or $K^{n+1} = \Phi$.

Step 3. Update variables.

$$Q^{n+1} = \begin{pmatrix} Q^n & \mathbf{0} \\ \mathbf{0}^T & 0 \end{pmatrix} + \eta \begin{pmatrix} \rho \\ -1 \end{pmatrix} (\rho^T \quad -1), \quad (3)$$

where $\rho = Q^n A_P^T A_K$, $\eta = (A_K^T A_P - A_K^T A_P \rho)^{-1}$ and A_K consists of those column vectors of A relating to the selected basis functions in K^{n+1} . The updating formula of S is

$$\begin{pmatrix} S_P^{n+1} \\ S_K^{n+1} \end{pmatrix} = \begin{pmatrix} S_P^n \\ \mathbf{0} \end{pmatrix} + \begin{pmatrix} \rho \eta \Delta \\ -\eta \Delta \end{pmatrix}, \quad (4)$$

where $\Delta = \rho^T (A_P^T \Phi^m - \lambda \nu_P / 2) - A_K^T \Phi^m + \lambda \nu_K / 2$.

Step 4. $O = O - K^{n+1}$, and $P = P + K^{n+1}$.

Step 5. $n = n + 1$, go to Step 1.

After the inversion on Θ_i ($i = 1, 2, 3, \dots$) completes, adaptive mesh refinement is triggered. All of the elements

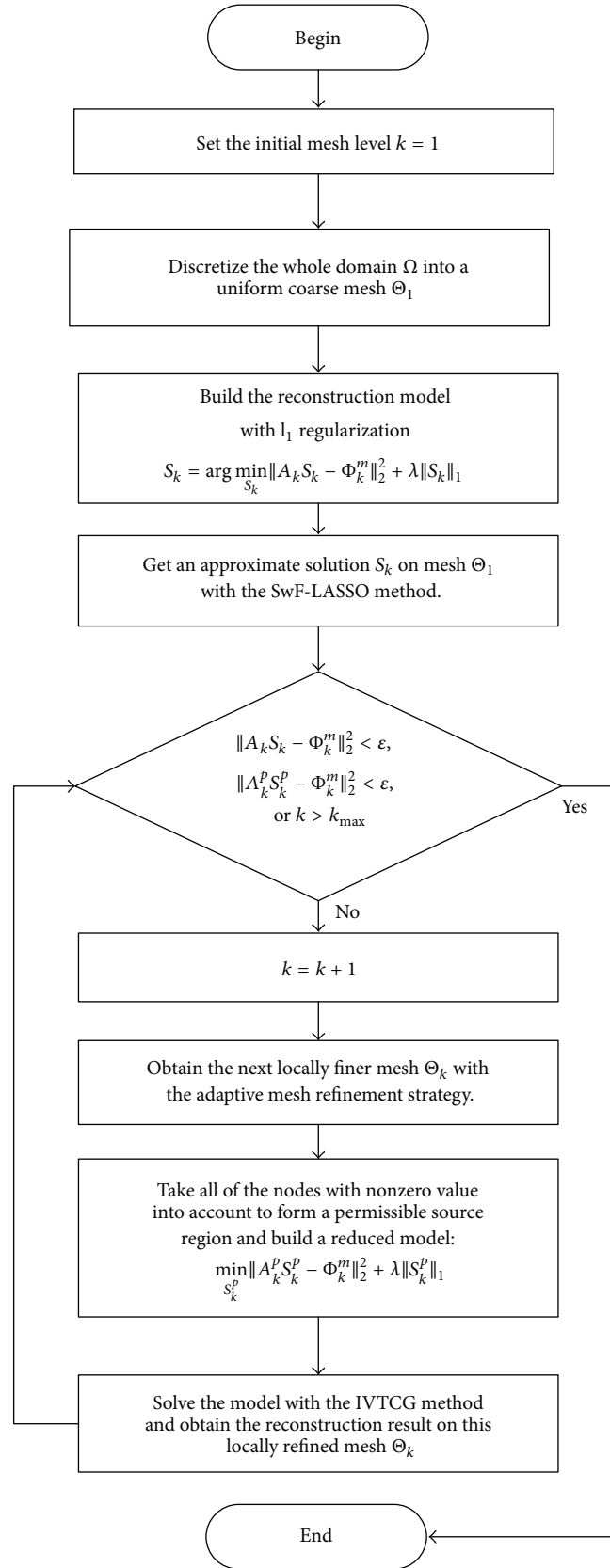


FIGURE 1: Flow chat of the hybrid multilevel reconstructions method.

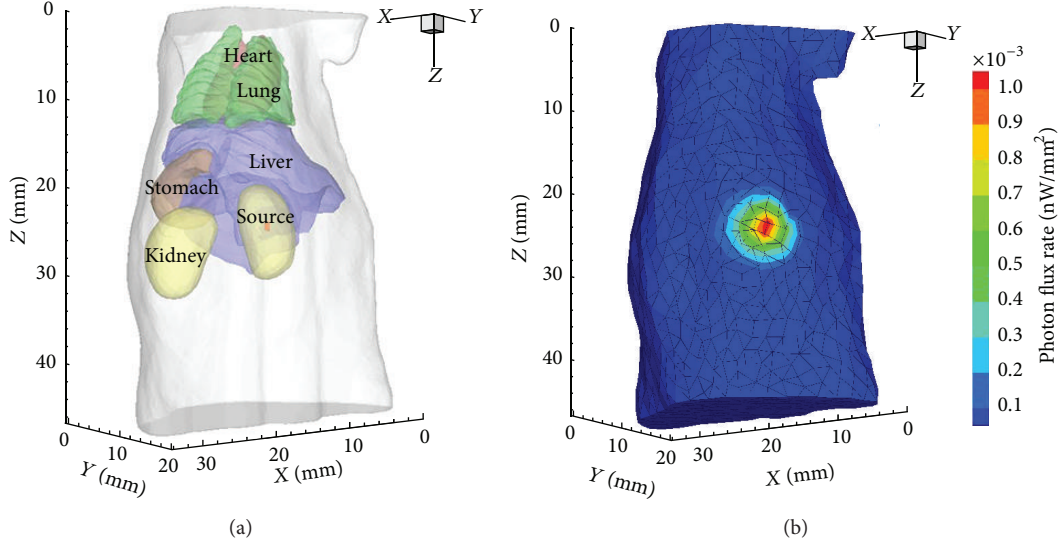


FIGURE 2: (a) The torso of the mouse atlas model with a cylindrical source in the right kidney. (b) Initial mesh for reconstruction and the simulated photon distribution on surface.

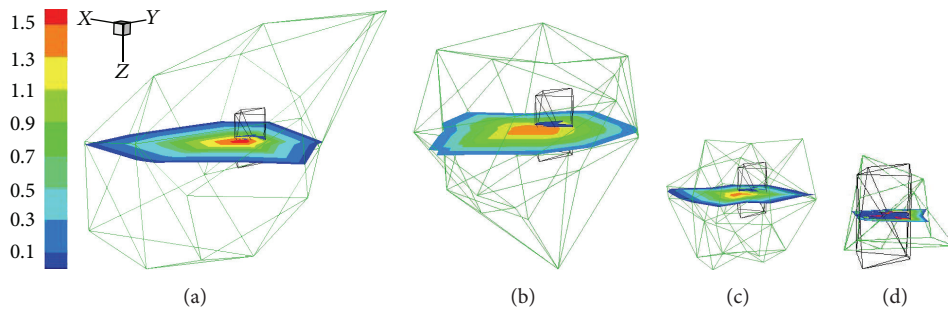


FIGURE 3: Evolution of reconstruction results with the local refined mesh in the single-source case. The green mesh denotes the local region that consists of nonzero nodes of the solution; the black mesh is the discretized source. (a) to (d) corresponds to four mesh levels, that is, Θ_1 to Θ_4 .

with nonzero reconstructed value are selected to be refined, which can be regarded as a kind of mesh refinement strategy based on *posteriori* error estimation. Using the longest-edge bisection method, a locally refined mesh Θ_{i+1} is obtained [17].

Unlike other previous reports, we employ a different reconstruction procedure on the succeeding mesh levels Θ_i ($i > 1$). The IVTCG algorithm proposed in [23] has been demonstrated as an effective reconstruction method by reformulating (2) as a convex quadratic program with nonnegative constrained conditions. It updates only partial variables in working set per iteration and adopts a working set splitting strategy to find the searching direction more efficiently, which leads to a small subproblem to be minimized and greatly decreases the number of iterations. The model transformation and the mechanism of IVTCG are detailed in [23].

We note that it is the sparseness-related parameter N_s that controls the size of the subproblem, which is solved by the truncated conjugate gradient method. Generally, for a very sparse problem, IVTCG can obtain accurate results with reasonable computational efficiency by setting $N_s =$

$\lfloor M/10 \rfloor$ and the maximum iterate number of the subproblem $\text{iter}_{\max} = N_s$. However, in the reconstruction procedures after local mesh refinement, the target is not a very sparse signal and the computational cost will increase sharply. In view of this feature, we make a modification and adjust the parameter $N_s = \lfloor M/4 \rfloor$, and $\text{iter}_{\max} = 25$ in our implementation.

A new round of local mesh refinement and reconstruction will be performed until the number of refinement exceeds the maximum number k_{\max} or the model misfit $\|AS - \Phi^m\|_2^2$ is reduced below a prespecified threshold ϵ . For the results reported in this work, we used $k_{\max} = 4$ and $\epsilon = 10^{-5}$.

The procedure of the proposed hybrid multilevel reconstructions method is illustrated in Figure 1.

3. Numerical Experiments and Results

We tested the proposed hybrid multilevel reconstruction method with a digital mouse model employing synthetically generated data. In the following simulations, we employed a 3D mouse atlas of CT and cryosection data to provide

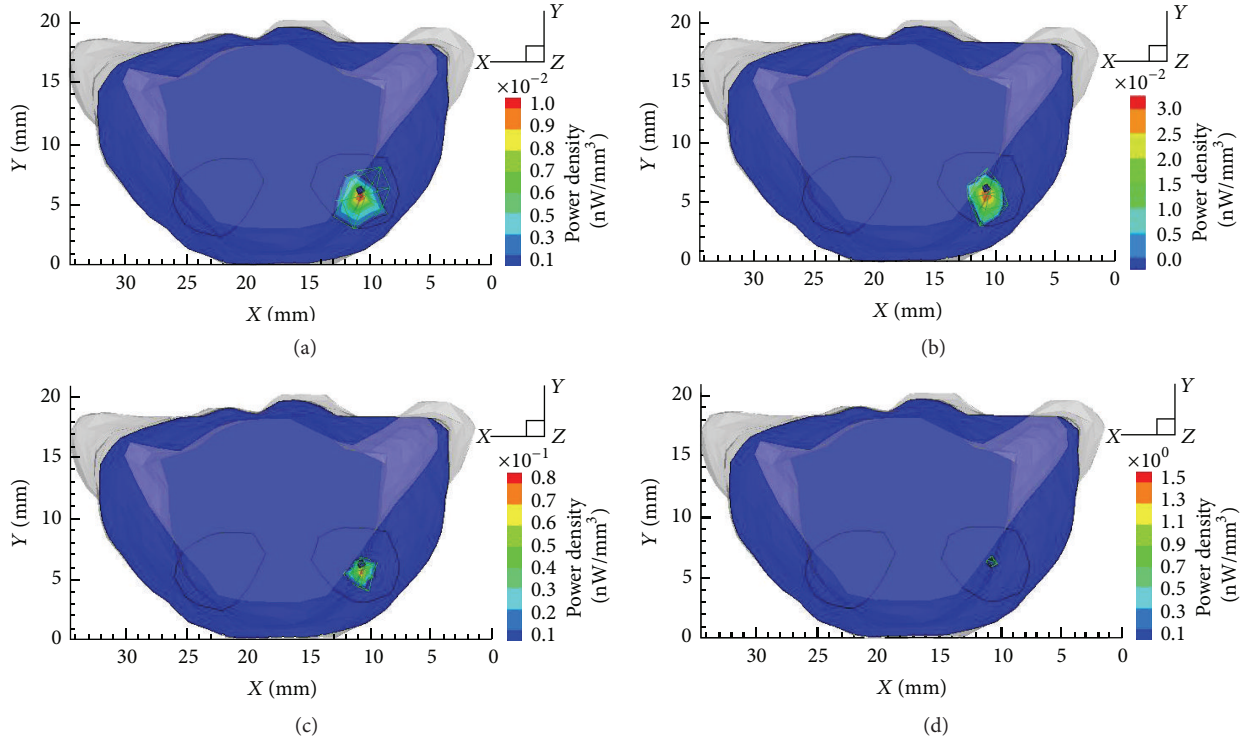


FIGURE 4: From (a) to (d): transverse views at $z = 25$ mm of the reconstruction results on mesh Θ_1 to mesh Θ_4 in single source, respectively.

anatomical information [26]. The CT slices of the mouse were segmented into major anatomical components, including lungs, a heart, a liver, a stomach, kidneys, and muscles. The corresponding optical properties were the same as the settings in [27], as shown in Table 1. The whole region included the mouse torso with a height of 45 mm.

In the following numerical experiments, the torso model was discretized into a tetrahedral-element mesh, and synthetic measurements were generated by solving the forward model with FEM. To simulate the noise involved in real BLT experiments, 15% Gaussian white noise was added to the synthetic data. The qualities of the reconstruction are quantitatively assessed in terms of location error (LE) and relative error (RE) between the reconstructed power and the actual value.

3.1. Single-Target Reconstruction. In the first set of experiments, a cylindrical source with 0.4 mm radius and 1 mm height was positioned in the right kidney with the center at (11, 6, 25), as shown in Figure 2(a). The actual source power was 0.2299 nW after discretization with FEM. Figure 2(b) shows the initial mesh for reconstruction and the photon distribution on the surface.

Following the proposed hybrid multilevel reconstructions method, the final result in single-source case was obtained by four rounds of reconstructions. Figure 3 shows the refinement of local mesh around targets and the solution

TABLE 1: Optical properties for the atlas organs region.

Material	Muscle	Lungs	Heart	Liver	Kidney	Stomach
μ_a [mm^{-1}]	0.23	0.35	0.11	0.45	0.12	0.21
μ'_s [mm^{-1}]	1.00	2.30	1.10	2.00	1.20	1.70

progress from mesh Θ_1 to mesh Θ_4 . According to the proposed methods, fine resolution only presents around targets, while coarser resolution retains in other regions, which contributes to reaching the desirable resolution at acceptable computational cost. Figures 4 and 5 are the transverse views and 3D views of reconstruction results from mesh Θ_1 to mesh Θ_4 , which illustrate the improvement of results during adaptive mesh refinement.

To demonstrate the necessity and effectiveness of the hybrid reconstruction scheme, we first compared the SwF-LASSO and IVTCG method on the initial coarse mesh Θ_1 , and then we compared the results of hybrid method, that is, SwF-LASSO + IVTCG, with that of only using SwF-LASSO on the succeeding mesh levels. The detailed reconstruction results are presented in Table 2. Obviously, the reconstruction results by IVTCG are inferior to that of SwF-LASSO on Θ_1 , and hybrid AFEM scheme performs better than the traditional AFEM that uses monoalgorithm of SwF-LASSO on the subsequent mesh Θ_2 to mesh Θ_4 .

Owing to the hybrid multilevel reconstruction scheme, the location error and the relative error of power distinctly

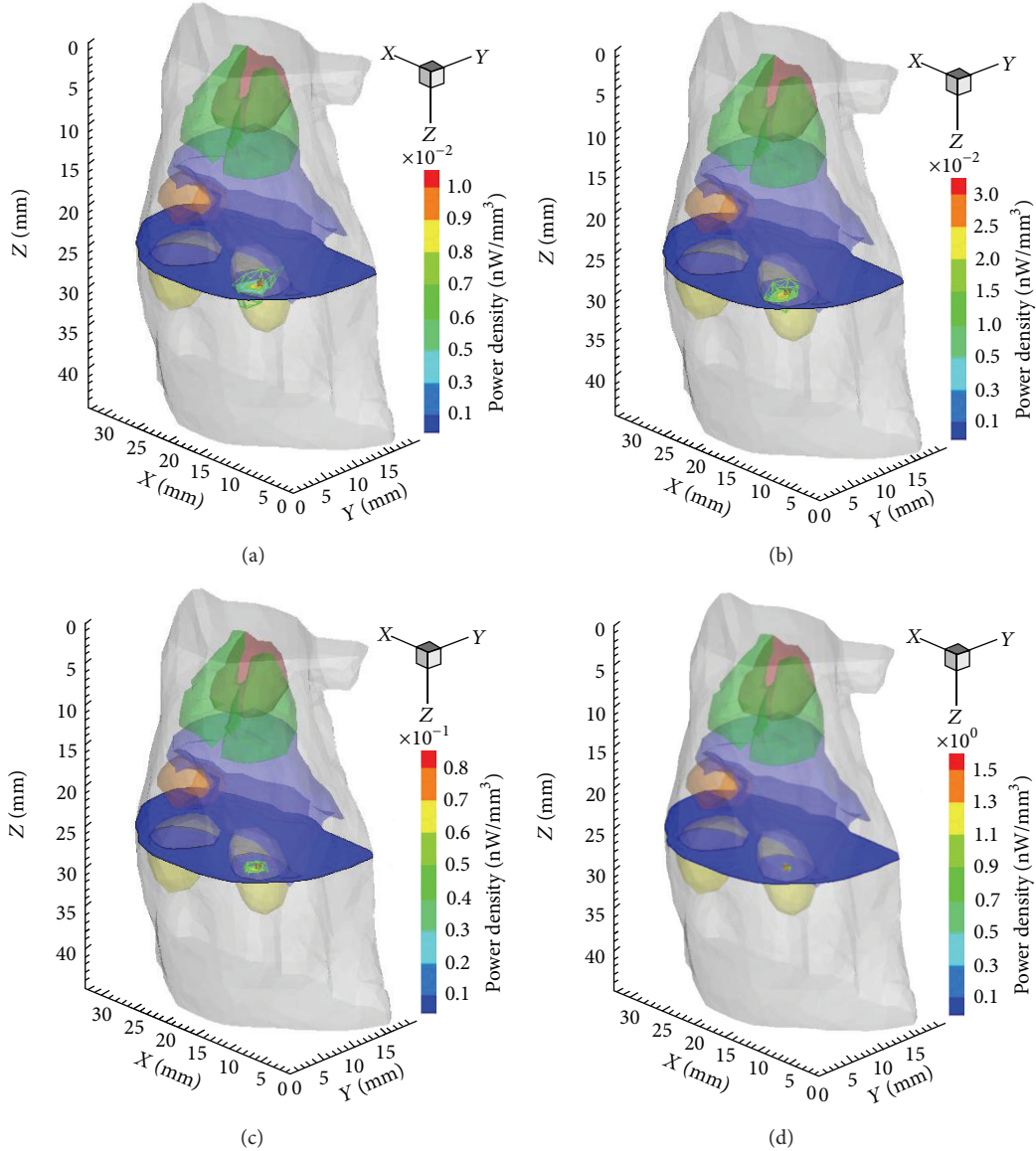


FIGURE 5: 3D views of the reconstruction results on mesh Θ_1 to mesh Θ_4 in single source.

decrease with the adaptively local mesh refinement. Especially, significant improvement of reconstructed density and power can be seen from the results in Table 2 and Figure 4.

3.2. Double-Source Reconstruction. We also investigated the resolving ability of the proposed method with two closely separated sources. Two cylindrical sources, same as that in the above single-target setting, were located in the right kidney with their centers at (9, 6.5, 25) and (12, 4, 25), respectively. They were identical in size and density, but the initial powers of them were 0.2120 nW and 0.2250 nW, mainly due to the influence of the mesh. The source setting and the simulated photon distribution are shown in Figure 6.

In double-source case, the multilevel reconstruction terminated on the third mesh level Θ_3 . Figure 7 displays the reconstruction results by the proposed method on mesh Θ_1

and mesh Θ_3 . The final result of the traditional AFEM, only using SwF-LASSO as the inversion algorithm on each mesh level, is also shown in Figures 7(c) and 7(f) for comparison. More detailed quantitative results are summarized in Table 3.

Figure 7 witnesses an apparent advantage of using hybrid scheme. Although the first-round result was biased towards a node between the targets on mesh Θ_1 , the proposed method successfully identified the two targets finally, which should be attributed to both the AFEM and the hybrid strategy. By contrasting Figure 7(d) with Figure 7(e), we can observe that the improvement caused by multilevel reconstruction with AFEM is evident. Nevertheless the final result of using monoalgorithm of SwF-LASSO is obviously inferior to that of using hybrid algorithm in terms of location accuracy and the reconstructed power error. Take source 1 for instance,

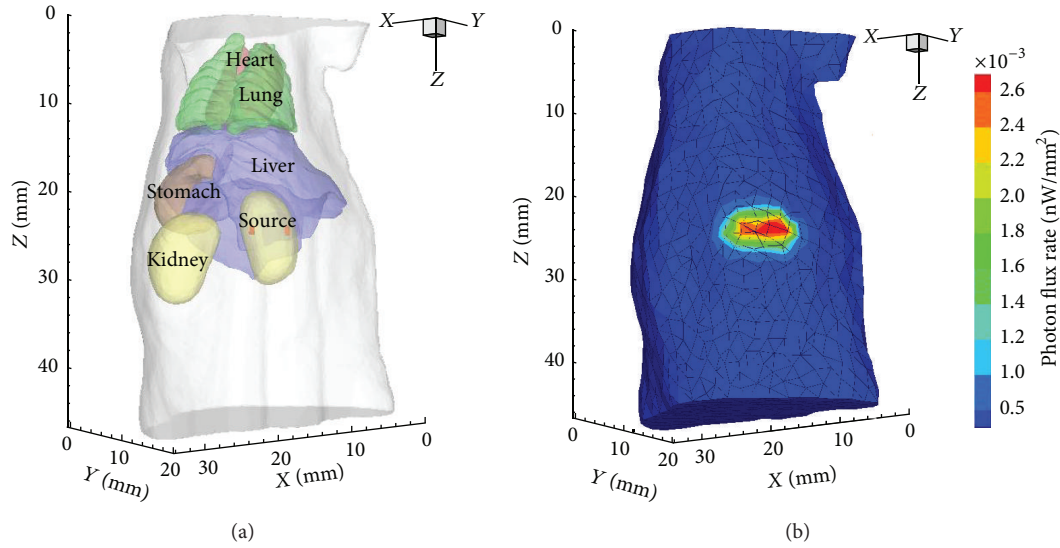


FIGURE 6: (a) Source setting in double-source case. (b) Initial mesh for reconstruction and the simulated photon distribution on surface.

TABLE 2: Reconstruction results in single-source case on different mesh levels.

Mesh	Recon. method	Recon. location (mm)	LE (mm)	Power (nW)	RE (%)
Θ_1	SwF-LASSO	11.02, 5.45, 25.18	0.58	0.1409	38.71
	IVTCG	10.60, 5.38, 27.00	2.13	0.0514	77.64
Θ_2	SwF-LASSO	11.02, 5.45, 25.18	0.58	0.1711	25.58
	Hybrid method	11.02, 5.45, 25.18	0.58	0.1773	22.88
Θ_3	SwF-LASSO	11.02, 5.45, 25.18	0.58	0.1765	23.23
	Hybrid method	11.02, 5.45, 25.18	0.58	0.1861	19.05
Θ_4	SwF-LASSO	11.00, 5.99, 25.01	0.01	0.1834	20.23
	Hybrid method	11.00, 5.99, 25.01	0.01	0.2529	10.00

the LE of the hybrid scheme reduces by 0.19 mm and the RE of power falls down to 2.3%. As for source 2, the proposed hybrid reconstruction method yields a 78% plunge in relative error of power.

4. In Vivo Experiments

To further validate the proposed method, an *in vivo* experiment was performed on an adult nude mouse. The animal procedures were in accordance with the Fourth Military Medical University that approved the animal protocol.

In the *in vivo* experiment, a capillary approximately 1.25 mm in diameter and 4.08 mm in length was inserted into the abdomen of the nude mouse. The capillary filled with 5 μ L luminescent liquid served as the testing source in this experiment. The luminescent solution was extracted from a red luminescent light stick (Glow products, Victoria, Canada), and the generated luminescent light had an emission peak wavelength of about 644 nm. The initial total power was 300 nW (the total power = luminescent solution volume \times luminescent solution flux density = 5 μ L \times 60 nW/ μ L).

This set of BLT experiments were conducted with a dual-modality BLT/micro-CT system [23]. The anesthetized mouse was first photographed, and luminescent images were taken by a calibrated CCD camera from four directions at 90 degree intervals with different exposure times. The multi-view superimposed photographs and luminescent images are shown in Figures 8(a)–8(d).

After the optical data were acquired, the intact mouse was scanned using the Micro-CT. Because of the limited field of view, only the torso section was scanned. The volume data were reconstructed using GPU-accelerated FDK algorithm [28]. From the CT slices, we located the center coordinate (21.44, 27.52, 9.76) of the actual luminescent source. The mouse body was segmented into five anatomical components, including muscle, heart, lungs, liver, and kidneys. The relevant optical properties of the mouse are listed in Table 4 [29].

Based on the collected multiview luminescent images and the volume data of CT, the 3D surface distribution is determined by the mapping algorithm described in [30], as shown in Figure 8(e). After the mapping process, three rounds of

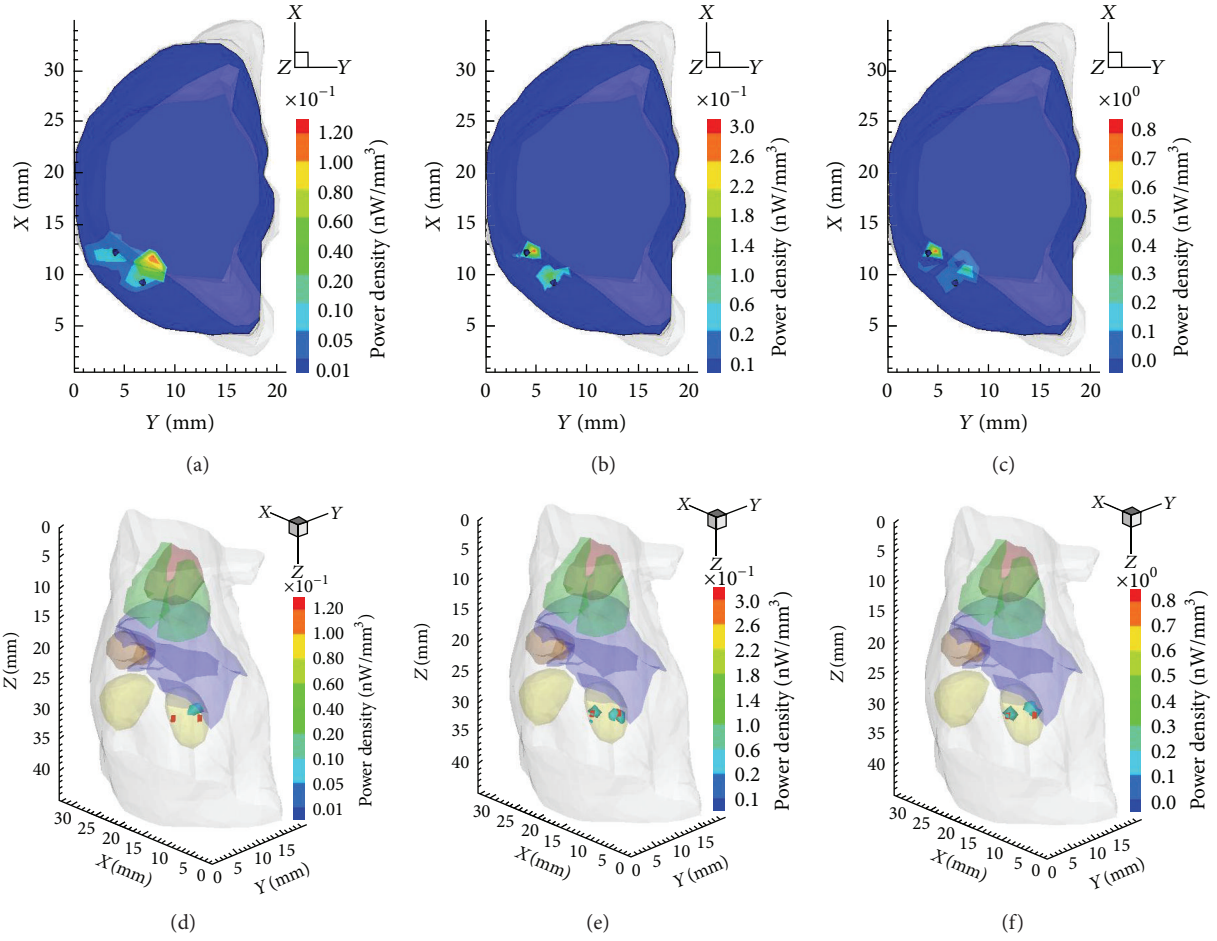


FIGURE 7: Top row: transverse views of reconstruction results in double-source case at $z = 25$ mm. Bottom row: 3D views. (a) and (d) are the first-round results on mesh Θ_1 , (b) and (e) are the final results of the proposed hybrid method, (c) and (f) are the final reconstruction results by the monoalgorithm of SwF-LASSO.

TABLE 3: Reconstruction results on different mesh levels in double-source case.

Mesh	Recon. method	Source ID	Recon. location (mm)	LE (mm)	Power (nW)	RE (%)
Θ_1	SwF-LASSO	1	10.96, 7.63, 24.52	2.31	0.5231	147.5
		2	10.96, 7.63, 24.52	3.81	0.5231	132.5
Θ_2	Only SwF-LASSO	1	9.98, 7.58, 25.33	1.50	0.3337	57.4
		2	12.09, 4.66, 25.06	0.67	0.5805	158
Θ_2	Hybrid method	1	9.70, 6.14, 25.10	0.79	0.2208	4.2
		2	12.09, 4.66, 25.06	0.67	0.2083	7.4
Θ_3	Only SwF-LASSO	1	9.70, 6.14, 25.10	0.79	0.2894	36.5
		2	12.09, 4.66, 25.06	0.67	0.4393	95.2
Θ_3	Hybrid method	1	8.80, 5.94, 24.91	0.60	0.2168	2.3
		2	12.09, 4.66, 25.06	0.67	0.2638	17.2

reconstructions on gradually refined meshes were performed with the proposed hybrid method. The reconstruction result on mesh Θ_1 is presented in Figure 9, where the source center is (20.39, 27.98, 9.78) with a deviation of 1.15 mm to the actual center. From mesh Θ_1 to mesh Θ_3 , the source locations are

identical, which means that the SwF-LASSO algorithm yields relatively accurate location from the beginning. However, the preliminary reconstruction on the initial coarse mesh Θ_1 possesses relative bigger errors in source power. After two rounds of local mesh refinement, the final results of hybrid method

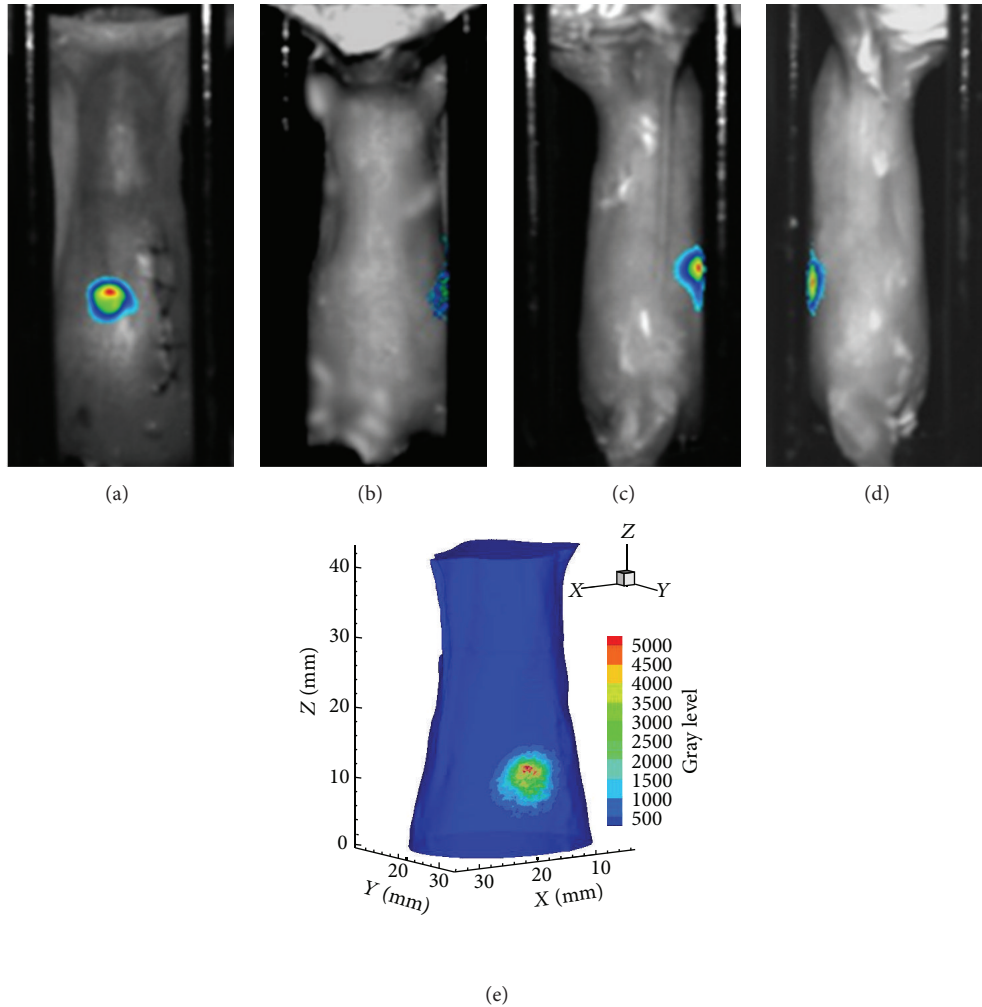


FIGURE 8: (a)–(d) are multiview superimposed images of photographs and luminescent images, and (e) is the surface mapping result before reconstruction.

TABLE 4: Optical properties of the living nude mouse.

Material	Muscle	Lungs	Heart	Liver	Kidney
μ_a [mm^{-1}]	0.009	0.460	0.138	0.829	0.155
μ'_s [mm^{-1}]	1.258	2.265	1.077	0.736	2.533

improved prominently. Specifically, the reconstructed power increased from 149.01 nW to 214.60 nW, and the RE of power decreased from 50.33% to 28.47%. The 3D views of the corresponding results on mesh Θ_1 to mesh Θ_3 are presented in Figure 10.

5. Discussion and Conclusion

We present a novel multilevel reconstruction method for whole domain BLT, which combines the merit of sparse regularization with the advantage of adaptive FEM. Numerical experiment results employing synthetic data with a digital mouse model illustrate that the proposed hybrid multilevel reconstruction scheme is able to accurately localize and

quantify source distribution without *a priori* information of permissible source region and multispectral measurements. The *in vivo* experiments conducted on a nude mouse with a dual-modality BLT/micro-CT system further validate the proposed method.

From the above experiments, we can find that the inversion algorithm on the initial coarse mesh has more important impact on the final result in the proposed hybrid scheme. The SwF-LASSO algorithm is able to provide a good initial localization with better numerical stability, which guides the subsequent reconstruction on finer meshes to obtain more accurate location and power. Furthermore, the experimental results also demonstrate that the hybrid strategy works. Compared with the multilevel reconstruction using monoalgorithm, the hybrid scheme performs better especially for multiple targets reconstruction. Therefore, it is also possible to form another qualified hybrid scheme using some other promising inversion algorithms.

For the sake of computational efficiency, the reconstructions presented in this paper are based on the diffusion equation. Therefore, the inadequately accurate forward

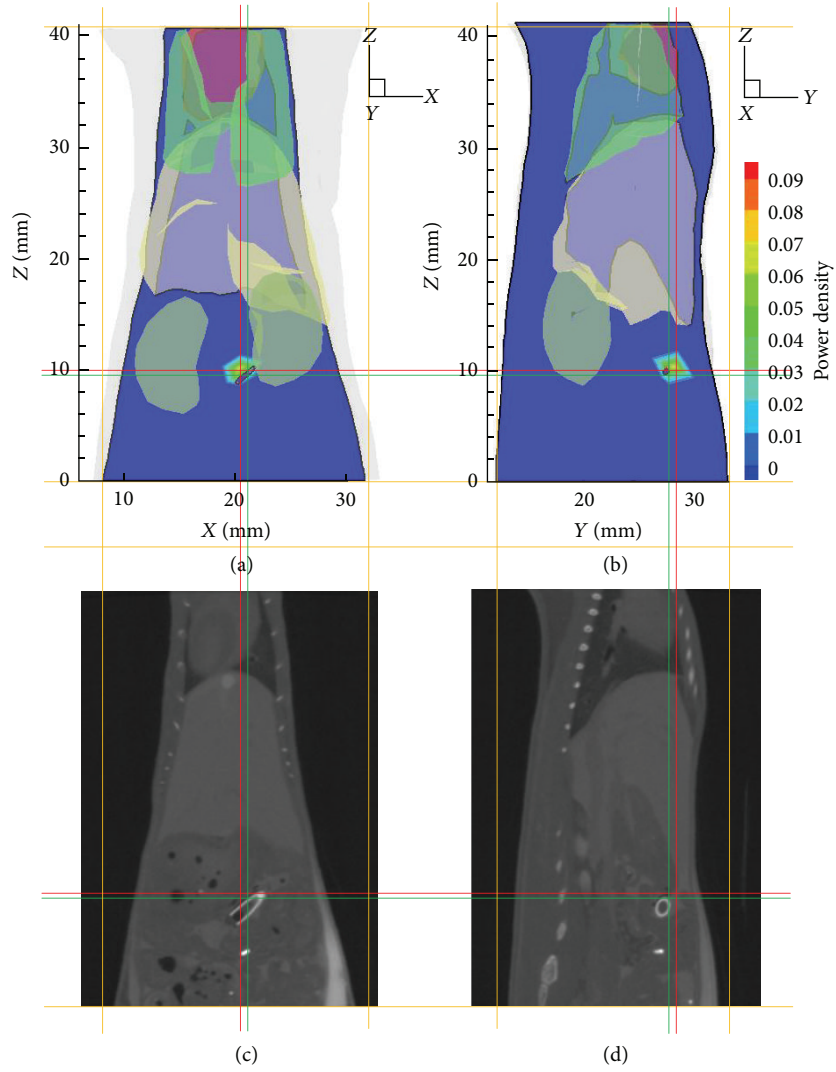


FIGURE 9: The transverse view of the reconstruction result and the comparison with the corresponding CT slices. The cross of the green lines denotes the actual source center, and the cross of the red lines denotes the reconstructed center.

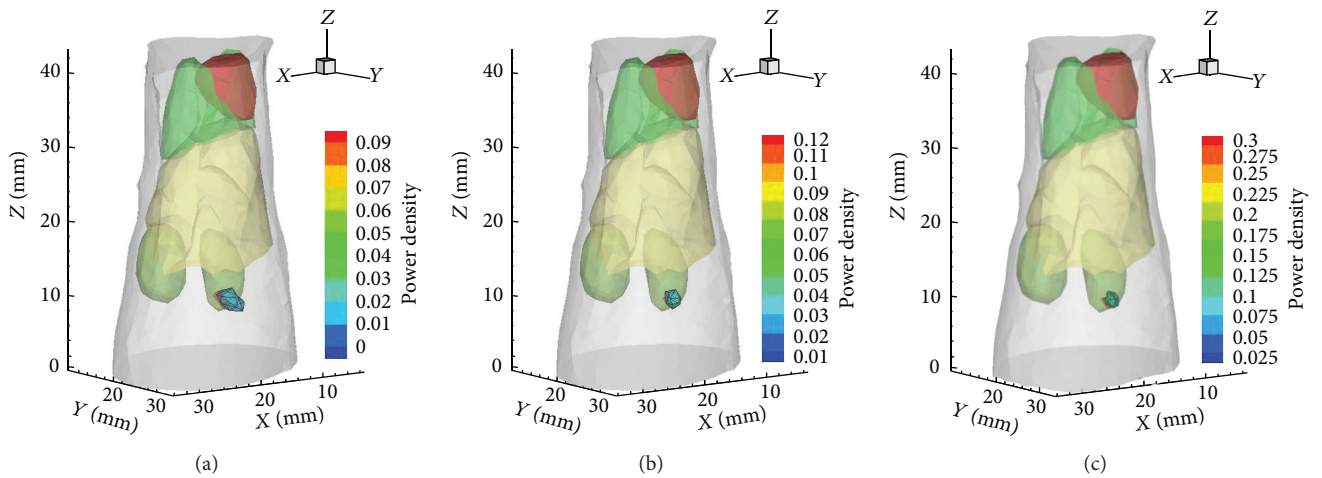


FIGURE 10: (a)–(c) are the reconstruction results for *in vivo* data on mesh Θ_1 to mesh Θ_3 .

model also leads to some inevitable error. The reconstruction performance might be further improved by using more accurate models, which is also the direction of our further work.

In addition to the many advantages of adaptive finite element methods, such as providing fine resolution around targets with coarser resolution in other region, the proposed hybrid scheme has two remarkable features. (i) Reconstruction result evolves adaptively with iterations, and the reconstruction accuracy is easily controlled by users. (ii) The inversion techniques employed on the initial coarse mesh and the succeeding ones vary with the discretization level to maintain solution stability and computational efficiency.

Acknowledgments

This work is supported by the National Basic Research Program of China (no. 2011CB311802), the Specialized Research Fund for the Doctoral Program of Higher Education of China (New Teachers) (no. 20116101120018), the China Postdoctoral Science Foundation Funded Project (nos. 2011M501467 and 2012T50814), the Natural Science Basic Research Plan in Shaanxi Province of China (nos. 2011JQ8029 and 2011JQ1006), the Science and Technology Plan Program in Shaanxi Province of China (New Scientific and Technological Star) (no. 2012 KJXX-29).

References

- [1] V. Ntziachristos, J. Ripoll, L. V. Wang, and R. Weissleder, "Looking and listening to light: the evolution of whole-body photonic imaging," *Nature Biotechnology*, vol. 23, no. 3, pp. 313–320, 2005.
- [2] R. Weissleder and M. J. Pittet, "Imaging in the era of molecular oncology," *Nature*, vol. 452, no. 7187, pp. 580–589, 2008.
- [3] J. K. Willmann, N. van Bruggen, L. M. Dinkelborg, and S. S. Gambhir, "Molecular imaging in drug development," *Nature Reviews Drug Discovery*, vol. 7, no. 7, pp. 591–607, 2008.
- [4] M. Hutchens and G. D. Luker, "Applications of bioluminescence imaging to the study of infectious diseases," *Cellular Microbiology*, vol. 9, no. 10, pp. 2315–2322, 2007.
- [5] C. H. Contag and M. H. Bachmann, "Advances in *in vivo* bioluminescence imaging of gene expression," *Annual Review of Biomedical Engineering*, vol. 4, pp. 235–260, 2002.
- [6] W. Cong, G. Wang, D. Kumar et al., "Practical reconstruction method for bioluminescence tomography," *Optics Express*, vol. 13, no. 18, pp. 6756–6771, 2005.
- [7] J. Tian, J. Bai, X. P. Yan et al., "Multimodality molecular imaging: improving image quality," *IEEE Engineering in Medicine and Biology Magazine*, vol. 27, no. 5, pp. 48–57, 2008.
- [8] G. Wang, Y. Li, and M. Jiang, "Uniqueness theorems in bioluminescence tomography," *Medical Physics*, vol. 31, pp. 2289–2299, 2004.
- [9] H. Dehghani, S. C. Davis, and B. W. Pogue, "Spectrally resolved bioluminescence tomography using the reciprocity approach," *Medical Physics*, vol. 35, no. 11, pp. 4863–4871, 2008.
- [10] Y. Lu, X. Zhang, A. Douraghy et al., "Source reconstruction for spectrally-resolved bioluminescence tomography with sparse *a priori* information," *Optics Express*, vol. 17, no. 10, pp. 8062–8080, 2009.
- [11] A. J. Chaudhari, F. Darvas, J. R. Bading et al., "Hyperspectral and multispectral bioluminescence optical tomography for small animal imaging," *Physics in Medicine and Biology*, vol. 50, no. 23, pp. 5421–5441, 2005.
- [12] A. X. Cong and G. Wang, "Multispectral bioluminescence tomography: methodology and simulation," *International Journal of Biomedical Imaging*, vol. 2006, Article ID 57614, 7 pages, 2006.
- [13] C. Qin, S. Zhu, J. Feng et al., "Comparison of permissible source region and multispectral data using efficient bioluminescence tomography method," *Journal of Biophotonics*, vol. 4, no. 11-12, pp. 824–839, 2011.
- [14] J. Yu, F. Liu, L. C. Jiao, S. Yang, and X. He, "A finite element meshes aggregating approach to multiple-source reconstruction in bioluminescence tomography," *International Journal of Biomedical Imaging*, vol. 2011, Article ID 210428, 12 pages, 2011.
- [15] Y. Lv, J. Tian, W. Cong et al., "A multilevel adaptive finite element algorithm for bioluminescence tomography," *Optics Express*, vol. 14, no. 18, pp. 8211–8223, 2006.
- [16] R. H. Nochetto, K. G. Siebert, and A. Veiser, "Theory of adaptive finite element methods: an introduction," in *Multiscale, Nonlinear and Adaptive Approximation*, pp. 409–542, Springer, Berlin, Germany, 2009.
- [17] X. Song, D. Wang, N. Chen, J. Bai, and H. Wang, "Reconstruction for free-space fluorescence tomography using a novel hybrid adaptive finite element algorithm," *Optics Express*, vol. 15, no. 26, pp. 18300–18317, 2007.
- [18] Y. Lv, J. Tian, W. Cong et al., "A multilevel adaptive finite element algorithm for bioluminescence tomography," *Optics Express*, vol. 14, no. 18, pp. 8211–8223, 2006.
- [19] R. Han, J. Liang, X. Qu et al., "A source reconstruction algorithm based on adaptive *hp*-FEM for bioluminescence tomography," *Optics Express*, vol. 15, no. 18, pp. 11095–11116, 2009.
- [20] X. He, Y. Hou, D. Chen et al., "Sparse regularization-based reconstruction for bioluminescence tomography using a multilevel adaptive finite element method," *International Journal of Biomedical Imaging*, vol. 2011, Article ID 203537, 11 pages, 2011.
- [21] H. Gao and H. Zhao, "Multilevel bioluminescence tomography based on radiative transfer equation part 1: II regularization," *Optics Express*, vol. 18, no. 3, pp. 1854–1871, 2010.
- [22] J. Yu, F. Liu, J. Wu, L. Jiao, and X. He, "Fast source reconstruction for bioluminescence tomography based on sparse regularization," *IEEE Transactions on Biomedical Engineering*, vol. 57, no. 10, pp. 2583–2586, 2010.
- [23] X. He, J. Liang, X. Wang et al., "Sparse reconstruction for quantitative bioluminescence tomography based on the incomplete variables truncated conjugate gradient method," *Optics Express*, vol. 18, no. 24, pp. 24825–24841, 2010.
- [24] X. Zhang, Y. Lu, and T. Chan, "A novel sparsity reconstruction method from poisson data for 3D bioluminescence tomography," *Journal of Scientific Computing*, vol. 50, no. 3, pp. 519–535, 2012.
- [25] H. R. A. Basevi, K. M. Tichauer, F. Leblond et al., "Compressive sensing based reconstruction in bioluminescence tomography improves image resolution and robustness to noise," *Biomedical Optics Express*, vol. 3, no. 9, pp. 2131–2141, 2012.
- [26] B. Dogdas, D. Stout, A. F. Chatzioannou, and R. M. Leahy, "Digimouse: a 3D whole body mouse atlas from CT and cryosection data," *Physics in Medicine and Biology*, vol. 52, no. 3, pp. 577–587, 2007.

- [27] G. Wang, W. Cong, K. Durairaj et al., “*In vivo* mouse studies with bioluminescence tomography,” *Optics Express*, vol. 14, no. 17, pp. 7801–7809, 2006.
- [28] G. Yan, J. Tian, S. Zhu, Y. Dai, and C. Qin, “Fast cone-beam CT image reconstruction using GPU hardware,” *Journal of X-Ray Science and Technology*, vol. 16, no. 4, pp. 225–234, 2008.
- [29] G. Alexandrakis, F. R. Rannou, and A. F. Chatziioannou, “Tomographic bioluminescence imaging by use of a combined optical-PET (OPET) system: a computer simulation feasibility study,” *Physics in Medicine and Biology*, vol. 50, no. 17, pp. 4225–4241, 2005.
- [30] X. Chen, X. Gao, D. Chen et al., “3D reconstruction of light flux distribution on arbitrary surfaces from 2D multi-photographic images,” *Optics Express*, vol. 18, no. 19, pp. 19876–19893, 2010.

Research Article

Morphological Measurement of Living Cells in Methanol with Digital Holographic Microscopy

Yunxin Wang,^{1,2} Yishu Yang,³ Dayong Wang,^{1,2} Liting Ouyang,^{1,2}
Yizhuo Zhang,^{1,4} Jie Zhao,⁵ and Xinlong Wang^{1,2}

¹ College of Applied Sciences, Beijing University of Technology, Beijing 100124, China

² Institute of Information Photonics Technology, Beijing University of Technology, Beijing 100124, China

³ College of Life Science & Biotechnology, Beijing University of Technology, Beijing 100124, China

⁴ Beijing Aeronautical Manufacturing Technology Research Institute, AVIC, Beijing 100124, China

⁵ The Pilot College, Beijing University of Technology, Beijing 101101, China

Correspondence should be addressed to Dayong Wang; wdyong@bjut.edu.cn

Received 14 September 2012; Revised 16 December 2012; Accepted 18 December 2012

Academic Editor: Yujie Lu

Copyright © 2013 Yunxin Wang et al. This is an open access article distributed under the Creative Commons Attribution License, which permits unrestricted use, distribution, and reproduction in any medium, provided the original work is properly cited.

Cell morphology is the research foundation in many applications related to the estimation of cell status, drug response, and toxicity screening. In biomedical field, the quantitative phase detection is an inevitable trend for living cells. In this paper, the morphological change of HeLa cells treated with methanol of different concentrations is detected using digital holographic microscopy. The compact image-plane digital holographic system is designed based on fiber elements. The quantitative phase image of living cells is obtained in combination with numerical analysis. The statistical analysis shows that the area and average optical thickness of HeLa cells treated with 12.5% or 25% methanol reduce significantly, which indicates that the methanol with lower concentration could cause cellular shrinkage. The area of HeLa cells treated with 50% methanol is similar to that of normal cells ($P > 0.05$), which reveals the fixative effect of methanol with higher concentration. The maximum optical thickness of the cells treated with 12.5%, 25%, and 50% methanol is greater than that of untreated cells, which implies the pyknosis of HeLa cells under the effect of methanol. All of the results demonstrate that digital holographic microscopy has supplied a noninvasive imaging alternative to measure the morphological change of label-free living cells.

1. Introduction

Cell morphology closely related to its various functions and activities is the research foundation of the modern biomedical discipline and life science. Under the normal cell culture, the size of the living cell changes apparently due to cell proliferation or cell death, and the survival status of the cells can also be estimated by the cell morphology to a great extent. Apoptosis, as a process of the programmed cell death, plays an important role in the development and homeostasis, and the morphological change is a typical feature for distinguishing the apoptosis and necrosis [1, 2]. The cell morphology can also reveal how the living cells have been influenced by the different environmental factors or different medical treatments such as anticancer drugs [3, 4]. Besides,

in some diseases such as diabetes mellitus, iron deficiency anemia, and thalassemia, the cell morphology is significantly changed [5, 6]. Comparing with the simple observation, the quantitative phase detection for the morphological change of the label-free living cells has become an urgent demand for the biomedical research.

Optical microscopy is a major and powerful facility for the biological and medical study for several centuries. Since biological cells are nearly a kind of transparent objects called phase objects, the conventional intensity-based light microscopy imaging method hardly provides the adequate contrast between the cells and the environment. Fluorescence microscopy needs the exogenous label contrast agents such as rhodamine, acridine orange, green fluorescent protein (GFP) to solve the contrast problem, which may make the living

cells phototoxic and cytotoxic, and influence the cellular behavior unfortunately [7]. For these issues, many optical phase-imaging methods have been developed to achieve the label-free visual observation of living cells. The phase-contrast imaging techniques such as Zernike phase contrast microscope or differential interference contrast (DIC) microscope apparently increase the contrast of phase or semiphase objects; however, they are inherently qualitative approaches and cannot give the quantitative information of the subcellular structure. Therefore, several techniques have been developed to obtain the full-field and quantitative phase-contrast imaging, such as Fourier phase microscopy (FPM), Hilbert phase microscopy (HPM), diffraction phase microscopy (DPM), and digital holographic microscopy (DHM) [8–13]. Comparing with other imaging methods, DHM has attracted more attention of researches for its particular advantages. DHM can retrieve the quantitative amplitude and phase information of the object wavefront from a single digital hologram, which makes the real-time detection possible. Since the numerical focusing can be implemented by the wave propagation theory, DHM does not demand to strictly record the hologram in the focused image plane of the object, and the digital autofocus algorithm can help to search the best in-focused image. Furthermore, DHM does not need any complex scanning configuration and possesses a simple setup accordingly.

The noninvasive cell imaging based on DHM has attracted more attention in the biomedical field. Rappaz et al. measured the physiological parameters of the neurons and the testate amoebae by using premagnification digital holography [12, 13]. Kemper et al. studied the invasion mechanism of the living pancreas carcinoma cells and the interaction mechanism of the anticancer drug through the dynamic detection of living cells based on DHM system [14]. Kim et al. achieved the quantitative imaging of ovarian cancer cells through the angular spectrum method. Besides, they also quantitatively studied the wrinkling of a silicone rubber film by motile fibroblasts based on digital holography [15, 16]. Jeong et al. utilized the digital holographic optical coherence imaging to track the effect of cytoskeletal anticancer drugs on tissue inside its natural 3-dimension (3D) environment using time-course measurement of motility within tumor tissue [17]. Pavillon et al. applied the digital holographic microscopy to the early and label-free detection of cell death of the mouse cortical neurons [18]. However, it is also essential to develop the effective setup of DHM and expand its new applications.

The active ingredients of many drugs that are hardly soluble in water can only be dissolved in the organic solvents with high polarity [19, 20]. Methanol, as a kind of organic solvents, is often applied to the *in vitro* pharmacodynamic screening. Nevertheless, the methanol solution with high concentration has toxic effects on living cells; thus the methanol should be diluted to a low concentration when it is used for cell culture. In addition, the fixation of tissues and cells is a key process of immunohistochemistry. Methanol is a frequently used fixative with good penetration [21, 22]. It can remove the lipids leading to cellular dehydration, meanwhile, the proteins instantaneously precipitated on the cytoskeleton.

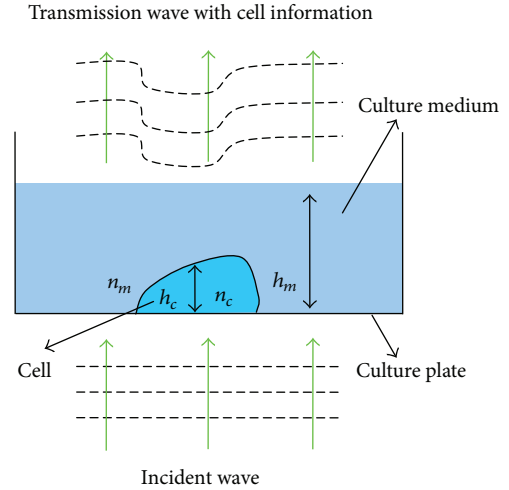


FIGURE 1: Schematic diagram of the phase imaging.

The fixative effects of methanol terminate or reduce the response of exogenous or endogenous enzymes to prevent autolysis of the cells in order to maintain the inherent shape and structure of the tissue cells, more importantly, to preserve antigenicity, and to prevent the loss or diffusion of antigen. In this paper, HeLa cells (human cervix carcinoma cell) are used as the tested sample. The cell morphological change treated with methanol solutions of different concentration is studied by the DHM imaging system. In combination with the numerical analysis and image processing, the surface area and optical thickness of cells are calculated, and the results show that the methanol solutions with different concentrations have diverse effects on the morphology of living HeLa cells.

2. Materials and Methods

2.1. Principle of Digital Holographic Microscopy. Digital holographic microscopy, as a quantitative phase-contrast imaging method, is essentially a kind of optical interferometry to detect the phase delay related to the light passing through the tested object. When passing through a relatively transparent sample, the intensity of the light changes very little, while the light through the sample speeds up or slows down and brings a corresponding phase change as indicated in Figure 1. The phase delay or advance depends on the relation of the refraction index between the sample and surrounding environment. Since the phase information is proportional to the optical path length called optical thickness, a depth profile of the tested sample can be calculated. Therefore, digital holography is particularly suitable to measure the phase object such as the living cells and microoptical elements.

In general, the coherent light source is divided into two arms, one arm goes through the tested object as the object beam, and the other one is used as the reference beam. The interference pattern of the object and reference beams is recorded by a high-resolution CCD detector to obtain the digital hologram represented by

$$I = |R|^2 + |O|^2 + R^*O + RO^*, \quad (1)$$

where O and R are the complex amplitude distributions for object and reference waves in the hologram plane, and $*$ denotes the complex conjugate operator.

As shown in (1), $|R|^2$ and $|O|^2$ is the dc term, R^*O is the real term, and RO^* is the virtual term. In the off-axis DHM configuration, the three terms are well separated, and the real term can be extracted by filtering in the frequency domain [23]. Then the real term R^*O can be propagated to the image plane using the diffraction theory. Various algorithms have been developed for the numerical reconstruction including Fresnel transform, convolution, and angular spectrum, all of which can be achieved with the help of fast Fourier transform (FFT), and we have analyzed the overlapping quality, accuracy, pixel resolution, computation window, and the speed of these methods [24]. The FFT-based angular spectrum method is used in this paper, which is superior to the FFT-based convolution method in the accuracy and speed. Different from the conventional optical holography, image processing technology can be combined to acquire the quantitative amplitude and phase distribution. In order to obtain the phase distribution from the digital hologram, it is essential to propagate the optical wave to different reconstructed distances to ensure the in-focus plane. The phase aberration induced by the tilted reference wave, microscopic objective (MO), and other optical elements can be corrected. Besides, the phase values are limited in the range of $(-\pi, +\pi)$ due to the principle of the arctan function, so the phase image will contain 2π discontinuities when the optical depth of test sample is greater than the wavelength λ . The least-squares phase-unwrapping algorithm is a good alternative to acquire the phase information [25]. After deducing the object complex amplitude distribution, we can obtain the phase-contrast image.

Next, the relation of the optical thickness and the physical thickness is discussed. For the adherent living cell is typically immersed in the cell culture solution as shown in Figure 1, the total optical path delay (OPD) of the transmission wave can be expressed as [12]:

$$\begin{aligned} \text{OPD}_t(x, y) &= (\bar{n}_c(x, y) - n_m)h_c(x, y) + n_m h_m \\ &= \text{OPD}_c(x, y) + \text{OPD}_m, \end{aligned} \quad (2)$$

where $\bar{n}_c(x, y)$ is the spatially varying integral refractive index, n_m is the refractive index of the culture solution, $h_c(x, y)$ is the spatially varying thickness of the cell, and h_m is the height of the culture solution. The integral refractive index $\bar{n}_c(x, y)$ is defined as follows:

$$\bar{n}_c(x, y) = \frac{1}{h_c(x, y)} \int_0^{h_c(x, y)} n_c(x, y, z) dz. \quad (3)$$

OPD_m is a reference OPD and can be measured in the place with no cells before calculating OPD_c . Then, OPD_c can be converted to the cell thickness distribution by

$$h_c(x, y) = \frac{\text{OPD}_c(x, y)}{\bar{n}_c(x, y) - n_m} \quad (4)$$

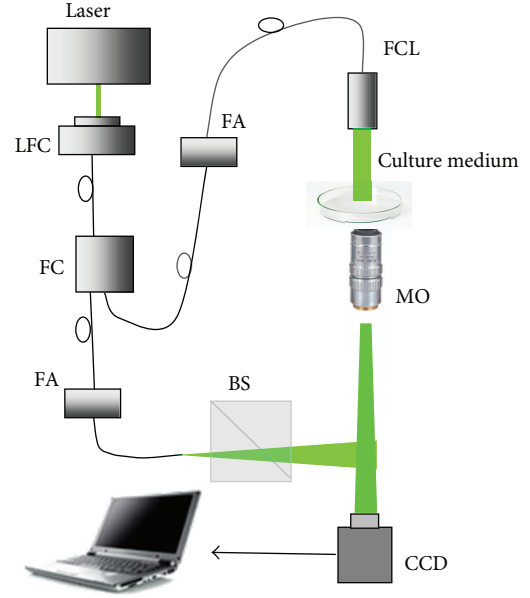


FIGURE 2: Schematic diagram of setup for the image-plane digital holographic microscopy.

Lue et al. and Jericho et al. have measured the refractive index of HeLa cells using Hilbert phase microscopy based on the microfluidic devices [26, 27], and the results indicated that the refractive index \bar{n}_c is 1.385 ± 0.047 . However, a change of the cellular refractive index may happen when seeding the HeLa cells in different culture medium [13, 28]; meanwhile, as seen from (4), $\bar{n}_c(x, y)$ is the function of the spatial coordinate, and the intracellular refractive such as the nucleoli and cytoplasm also possesses different refractive index. In view of the refractive index change caused by the intracellular refractive and the addition of different amounts of methanol in our experiment, we only give the optical thickness of HeLa cells to describe the morphological feature.

2.2. Digital Holographic System. Digital holographic setup can be simplified with the combination of the fiber [29–31]. The image-plane digital holographic microscopy setup is designed as illustrated in Figure 2. The laser source with a wavelength 532 nm is coupled into a fiber by a laser-to-fiber coupler (LFC) and then divided into two arms by a 1×2 fiber coupler (FC). A beam collimated by a fiber collimator (FCL) is employed as the object illumination beam, and the other one that is nearly spherical is used as the reference beam. The microscopic objective (20x, NA = 0.4) collects the light transmitted by the sample and produces a magnified real image on the image plane. The CCD camera is placed at the image plane of the object and records the digital hologram. The CCD camera can generate 1280×1024 pixel images with $4.65 \mu\text{m} \times 4.65 \mu\text{m}$ sized pixel. The reference light is reflected by a beam splitter (BS), which makes a small angle between the object beam and the reference beam. The two fiber attenuators (FA) in the object and reference arms are applied to adjust the intensity ratio to improve the image quality of digital hologram.

2.3. Sample Preparation. HeLa cells (from American Type Culture Collection) were maintained in Dulbecco's modified eagle medium (DMEM) supplemented with 10% (v/v) heat-inactivated fetal bovine serum (FBS), 100 units/mL penicillin, 100 mg/mL streptomycin, and 2 mM L-glutamine. The cells were incubated at 37°C with 5% CO₂. When the cell confluence reached about 90%, 0.25% trypsin solution was used to digest the cells for five minutes. Then 3.0×10^5 HeLa cells were seeded in 6-well plastic plates. Twenty-four hours after seeding, the cells were about 70% confluence. Methanol solution was serially diluted to 2-, 4-, or 8-fold using DMEM. The cultural supernatant was replaced with the diluted organic solvents or fresh DMEM. Three dilutions were applied, and four duplicates were adopted for each dilution. The concentration of methanol of each dilution was 12.5%, 25.0%, and 50% (v/v), respectively. The wells only with cells and without any organic solvent were used as cell control (CC). Twelve hours later, four samples are used for the morphological analysis of the living cells.

2.4. Digital Processing and Measurements. The hologram recorded by the image-plane digital holographic system is filtered in the frequency domain to remove the dc term and the virtual term. We adjusted CCD to the image plane of the object as much as possible in experiments, whereas it is inevitable that there may be a small distance between CCD and the exact image plane due to the limitation of the tuning component. To compensate the experimental error, the diffraction propagation within a distance ± 2 mm is applied to redefine the in-focus plane by angular spectrum algorithm. The phase aberration is corrected using the two-step phase subtraction method. In experiments, a reference hologram without the culture medium is recorded firstly, and then the phase images of the holograms with the culture medium can be acquired. It has been proved that it is sufficient to record a reference hologram prior to the measurement procedure to compensate the phase aberration [32]. Finally, the unwrapped phase image is obtained by the least-squares phase-unwrapping algorithm, and then the quantitative phase information of living cells can be obtained. In order to describe the morphological change of cells, the image segmentation is utilized to extract each cell from the phase image based on Matlab programs.

The process of the image segmentation is that firstly, the noises are reduced by the Gauss filter and median-filter with 5×5 pixels. There are usually a few tens of cells in a phase image, thus a small area including the interested cell is cut from the whole phase image to reduce the computational complexity and improve the accuracy of segmentation. Secondly, the image is enhanced by Sobel operator, and an adaptive threshold algorithm is adopted to transfer the phase image to a binary image. Considering the living cell is generally bigger than the discrete noises, so the connection area of a cell is larger than that of noises. According to this idea, the residual discrete noises can be mostly removed by detecting the pixel number of the connection area. Finally, we can label the location of the interested cell in the binary image. On the one hand, the surface area can be easily

calculated according to the total pixel number covered by the cell; on the other hand, we can also obtain the optical thickness of the cell. We pay more attention to the maximum optical thickness and average optical thickness of the cell. It is worth noting that the optical thickness of the cell is the difference between the thickness with cells and the reference thickness without cells. To increase the precision of optical thickness, the reference thickness is computed by averaging the optical thickness of several areas without cells.

3. Results and Discussion

In experiments, HeLa cells treated with different concentrations of methanol are imaged in the plastic plate. The morphology of untreated cells is illustrated in Figure 3(a). The cells are arranged regularly with the shape of polygon or diamond, which indicate that cells are mostly growing adherently in a healthy status. Besides, it is worth to note that the spontaneous death or aging of some cells may happen though cultured in a good condition. With the death of aging cells, the cells gradually lose the ability of adherent and become rounded under the surface tension in the solution. As shown in the dashed box of Figure 3(a), it is apparently a typical rounding death cell. Aiming to this kind of cells, not only the surface area changes into a round shape, but also the cell thickness has a visible change that can be supplied by digital holographic technology superiorly. For 18 normal cells in Figure 3(a), their average optical thickness \overline{OT} is 0.99 rad, and the average maximum optical thickness \overline{OT}_{\max} is 2.89 rad. Here, the average maximum optical thickness is defined as the average value of the maximum optical thickness of the counted cells. For the rounding cell in the dashed box, its average optical thickness \overline{OT} becomes higher up to 3.47 rad, and its maximum optical thickness OT_{\max} is 6.45 rad. Therefore, the oversize optical thickness may be a characterization of this kind of abnormal cells.

Methanol solutions with different concentrations have diverse effects on the morphology of living HeLa cells. Since the intermediate metabolite such as formaldehyde and formic acid caused by the excessive methanol will damage the cells to some extent. The cell morphologies treated with 12.5%, 25% and 50% methanol are shown in Figures 3(b), 3(c), and 3(d), respectively. We can see that the cell morphologies treated with methanol have obvious changes, especially the cell morphologies treated with 12.5% and 25% methanol.

The size distribution of 56 cells treated with 0% or 12.5% methanol is depicted in Figure 4 intuitively, where x and y coordinates represent the surface area (S) and the average optical thickness (\overline{OT}) of cells. Comparing Figure 4(a) with 4(b), both the cell area and average optical thickness distribute in a different interval, which imply the shape changes accordingly.

To describe the shape change quantitatively, the information of 56 cells are extracted from each concentration, and the parameters including area S , average optical thickness (\overline{OT}), average maximum optical thickness (\overline{OT}_{\max}), and the respective standard deviations (SD) are listed in Table 1. The

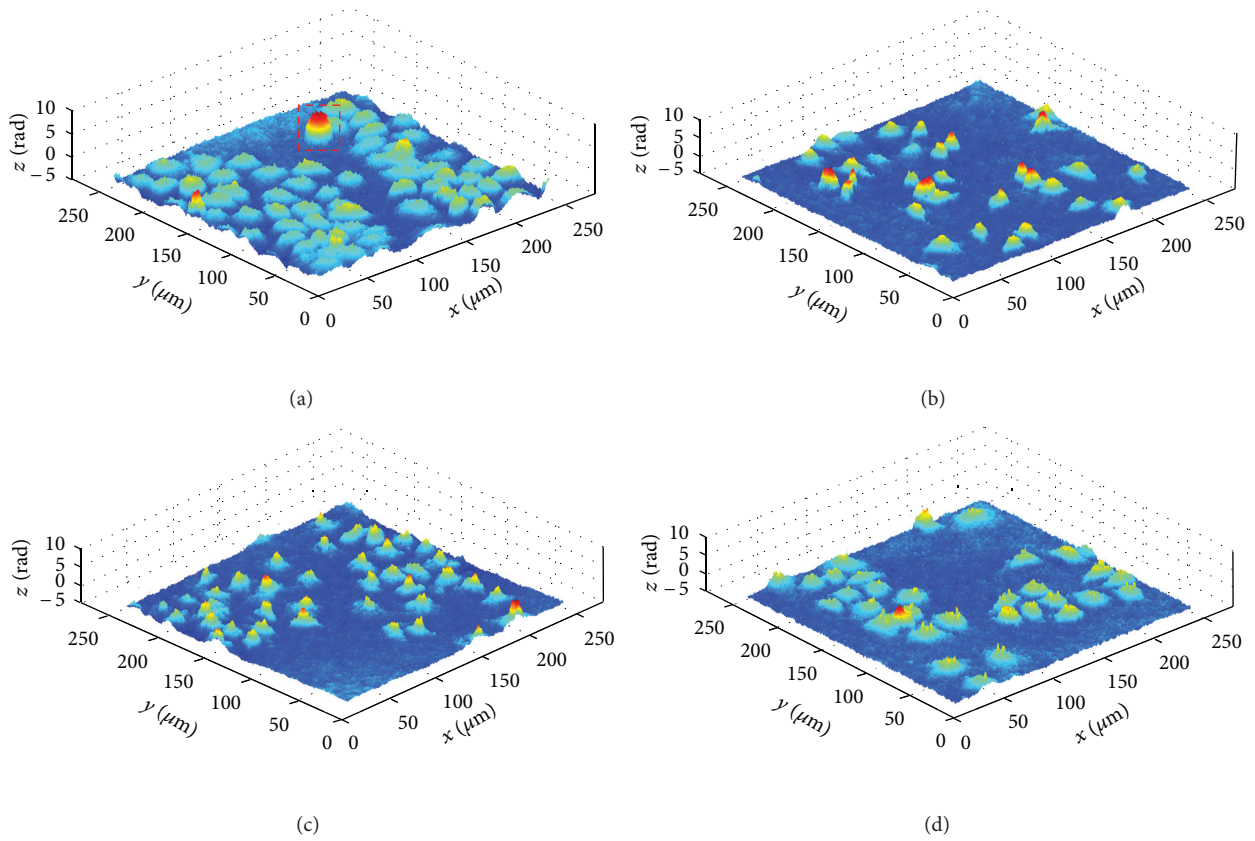


FIGURE 3: Phase-contrast imaging results of living cells after seeding 12 hours: (a) cell control; (b) treated with 12.5% methanol; (c) treated with 25% methanol; (d) treated with 50% methanol.

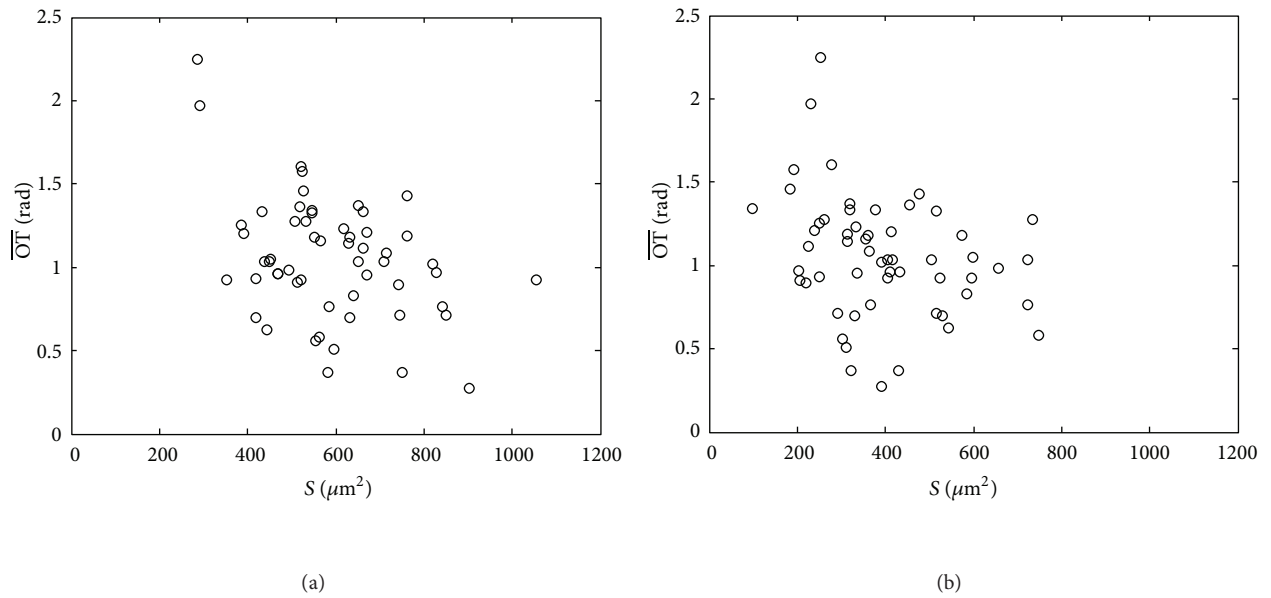


FIGURE 4: Size distribution of 56 cells: (a) cell control; (b) treated with 12.5% methanol.

TABLE 1: Data of the cell morphology with different methanol concentration.

Methanol concentration (%)	Parameters		
	$S (\mu\text{m}^2)$	\overline{OT} (rad)	\overline{OT}_{\max} (rad)
0 (CC)	590.3 ± 153.9	1.1 ± 0.4	3.1 ± 0.6
12.5	$394.8 \pm 152.8^{**}$	$0.8 \pm 0.4^{**}$	3.2 ± 0.7
25	$488.3 \pm 180.6^{**}$	$0.8 \pm 0.3^{**}$	$4.2 \pm 0.6^{**}$
50	574.0 ± 211.8	$1.3 \pm 0.4^{**}$	$4.1 \pm 0.6^{**}$

Remark: where $^{**}P < 0.01$ compared with the group of cell control.

statistical significance of experimental data is analyzed using t test and (analysis of variance) ANOVA based on Statistical Package for the Social Sciences (SPSS) Release 16.0. ANOVA shows significant differences existing in the above parameters between the four groups ($P < 0.01$). Then differences between the group of cell control and the group treated with methanol were probed. For HeLa cells treated with 12.5% or 25% methanol, the area is reduced significantly compared with that of the normal cells ($P < 0.01$), which indicates that the methanol with lower concentration could cause cellular shrinkage. For HeLa cells treated with 50% methanol, the area is similar with that of the normal cells ($P > 0.05$), which verifies the fixative effect of higher methanol concentration. However, there are still significant differences in both \overline{OT} and \overline{OT}_{\max} ($P < 0.01$) that can only be detected by phase image. The morphological feature of cells treated with 25% methanol shows significant differences in three parameters S , \overline{OT} , and \overline{OT}_{\max} ($P < 0.01$). Besides, the average maximum optical thickness of the cells treated with 12.5%, 25%, and 50% methanol is greater than that of untreated cells, which implies the pyknosis of HeLa cells under the effect of methanol.

4. Conclusions

It has been recently an urgent demand to quantitatively detect the morphology for living cells in the biomedical and life science field. In this paper, the morphological change of HeLa cells treated with the methanol solution is measured based on digital holographic microscopy. Methanol, as a kind of organic solvents, is often used to dissolve some drugs with low concentrations and also applied to the fixation of tissues and cells with high concentrations. After recording the hologram using the image-plane digital holographic system, the phase image of living cells is calculated by numerical analysis. With the assistance of the image processing, the surface area and optical thickness of the living cells are computed to describe the cell morphology quantitatively. The ANOVA shows significant differences between the four groups ($P < 0.01$). Compared with the CC group, S and \overline{OT} of HeLa cells treated with 12.5% or 25% methanol are reduced significantly, which verifies that the methanol with lower concentration has the toxic effects and could cause cellular shrinkage. For HeLa cells treated with 50% methanol, S is similar with that of the normal cells ($P > 0.05$), which reveals the fixative effect of methanol with higher concentration. Furthermore, \overline{OT}_{\max} of the cells treated with 12.5%, 25%, and 50% methanol is greater than that of untreated cells,

which implies the pyknosis of HeLa cells under the effect of methanol. All of the results demonstrate that digital holographic microscopy is a noninvasive imaging approach for detecting the morphological change of the label-free living cells.

Authors' Contribution

Y. Wang and Y. Yang contributed equally to this paper.

Acknowledgments

This work is financially supported by National Natural Science Foundation of China (nos. 61077004, 61107002, and 61205010), Beijing Municipal Natural Science Foundation (no. 1122004), and Research Fund for the Doctoral Program of Higher Education of China (no. 20121103120003).

References

- [1] A. L. Edinger and C. B. Thompson, "Death by design: apoptosis, necrosis and autophagy," *Current Opinion in Cell Biology*, vol. 16, no. 6, pp. 663–669, 2004.
- [2] N. Zucchini-Pascal, G. de Sousa, and R. Rahmani, "Lindane and cell death: at the crossroads between apoptosis, necrosis and autophagy," *Toxicology*, vol. 256, no. 1-2, pp. 32–41, 2009.
- [3] L. Zhang, W. Lei, X. Wang, Y. Tang, and J. Song, "Glucocorticoid induces mesenchymal-to-epithelial transition and inhibits TGF- β 1-induced epithelial-to-mesenchymal transition and cell migration," *FEBS Letters*, vol. 584, no. 22, pp. 4646–4654, 2010.
- [4] T. Kato, H. Fujino, S. Oyama, T. Kawashima, and T. Murayama, "Indomethacin induces cellular morphological change and migration via epithelial-mesenchymal transition in A549 human lung cancer cells: a novel cyclooxygenase-inhibition-independent effect," *Biochemical Pharmacology*, vol. 82, pp. 1781–1791, 2011.
- [5] R. Martínez-Tellez, M. d. Jesús Gómez-Villalobos, and G. Flores, "Alteration in dendritic morphology of cortical neurons in rats with diabetes mellitus induced by streptozotocin," *Brain Research*, vol. 1048, no. 1-2, pp. 108–115, 2005.
- [6] Y. Zhanga, W. Zhang, S. Wanga et al., "Detection of human erythrocytes influenced by iron deficiency anemia and thalassemia using atomic force microscopy," *Micron*, vol. 43, pp. 1287–1292, 2012.
- [7] L. J. Kricka and P. Fortina, "Analytical ancestry: "firsts" in fluorescent labeling of nucleosides, nucleotides, and nucleic acids," *Clinical Chemistry*, vol. 55, no. 4, pp. 670–683, 2009.

- [8] N. Lue, W. Choi, G. Popescu et al., "Quantitative phase imaging of live cells using fast Fourier phase microscopy," *Applied Optics*, vol. 46, no. 10, pp. 1836–1842, 2007.
- [9] T. Ikeda, G. Popescu, R. R. Dasari, and M. S. Feld, "Hilbert phase microscopy for investigating fast dynamics in transparent systems," *Optics Letters*, vol. 30, no. 10, pp. 1165–1167, 2005.
- [10] G. Popescu, T. Ikeda, R. R. Dasari, and M. S. Feld, "Diffraction phase microscopy for quantifying cell structure and dynamics," *Optics Letters*, vol. 31, no. 6, pp. 775–777, 2006.
- [11] B. Kemper and G. Von Bally, "Digital holographic microscopy for live cell applications and technical inspection," *Applied Optics*, vol. 47, no. 4, pp. A52–A61, 2008.
- [12] B. Rappaz, P. Marquet, E. Cuche, Y. Emery, C. Depeursinge, and P. J. Magistretti, "Measurement of the integral refractive index and dynamic cell morphometry of living cells with digital holographic microscopy," *Optics Express*, vol. 13, no. 23, pp. 9361–9373, 2005.
- [13] F. Charrière, N. Pavillon, T. Colomb et al., "Living specimen tomography by digital holographic microscopy: morphometry of testate amoeba," *Optics Express*, vol. 14, no. 16, pp. 7005–7013, 2006.
- [14] B. Kemper, D. Carl, J. Schnekenburger et al., "Investigation of living pancreas tumor cells by digital holographic microscopy," *Journal of Biomedical Optics*, vol. 11, no. 3, Article ID 034005, 2006.
- [15] C. J. Mann, L. Yu, C. M. Lo, and M. K. Kim, "High-resolution quantitative phase-contrast microscopy by digital holography," *Optics Express*, vol. 13, no. 22, pp. 8693–8698, 2005.
- [16] X. Yu, M. Cross, C. Liu, D. C. Clark, D. T. Haynie, and M. K. Kim, "Measurement of the traction force of biological cells by digital holography," *Biomedical Optics Express*, vol. 3, no. 1, pp. 153–159, 2012.
- [17] K. Jeong, J. J. Turek, and D. D. Nolte, "Volumetric motility-contrast imaging of tissue response to cytoskeletal anti-cancer drugs," *Optics Express*, vol. 15, no. 21, pp. 14057–14064, 2007.
- [18] N. Pavillon, J. Kühn, C. Moratal et al., "Early cell death detection with digital holographic microscopy," *PloS One*, vol. 7, no. 1, pp. 153–159, 2012.
- [19] Z. Liu, J. T. Robinson, X. Sun, and H. Dai, "PEGylated nanographene oxide for delivery of water-insoluble cancer drugs," *Journal of the American Chemical Society*, vol. 130, no. 33, pp. 10876–10877, 2008.
- [20] A. Avdeef, K. J. Box, J. E. A. Comer et al., "PH-metric logP 11. pK(a) determination of water-insoluble drugs in organic solvent-water mixtures," *Journal of Pharmaceutical and Biomedical Analysis*, vol. 20, no. 4, pp. 631–641, 1999.
- [21] Y. Qin and Y. Chen, "Effect of different fixatives on location of RhoA protein by immunofluorescence microscopy," *Journal of Jiangsu University*, vol. 16, no. 5, pp. 385–388, 2006.
- [22] J. Fan, N. Luo, X. Dong, and X. Yu, "Evaluation of different fixatives in confocal immunofluorescence," *Journal of Sun Yat-Sen University*, vol. 30, no. 5, pp. 600–604, 2009.
- [23] E. Cuche, P. Marquet, and C. Depeursinge, "Spatial filtering for zero-order and twin-image elimination in digital off-axis holography," *Applied Optics*, vol. 39, no. 23, pp. 4070–4075, 2000.
- [24] C. Liu, D. Wang, and Y. Zhang, "Comparison and verification of numerical reconstruction methods in digital holography," *Optical Engineering*, vol. 48, no. 10, Article ID 105802, 2009.
- [25] D. C. Ghiglia and M. D. Pritt, *Two-Dimensional Phase Unwrapping: Theory, Algorithms, and Software*, John Wiley & Sons, New York, NY, USA, 1998.
- [26] N. Lue, G. Popescu, T. Ikeda, R. R. Dasari, K. Badizadegan, and M. S. Feld, "Live cell refractometry using microfluidic devices," *Optics Letters*, vol. 31, no. 18, pp. 2759–2761, 2006.
- [27] M. H. Jericho, H. J. Kreuzer, M. Kanka, and R. Riesenberger, "Quantitative phase and refractive index measurements with point-source digital in-line holographic microscopy," *Applied Optics*, vol. 51, no. 10, pp. 1503–1515, 2012.
- [28] C. E. Rommel, C. Dierker, L. Schmidt et al., "Contrast-enhanced digital holographic imaging of cellular structures by manipulating the intracellular refractive index," *Journal of Biomedical Optics*, vol. 15, no. 4, Article ID 041509, 2010.
- [29] F. Pan, S. Liu, Z. Wang, P. Shang, and W. Xiao, "Digital holographic microscopy long-term and real-time monitoring of cell division and changes under simulated zero gravity," *Optics Express*, vol. 20, no. 10, pp. 11496–11505, 2012.
- [30] Y. Zhang, D. Wang, Y. Wang, and S. Tao, "Automatic compensation of total phase aberrations in digital holographic biological imaging," *Chinese Physics Letters*, vol. 28, no. 11, Article ID 114209, 2011.
- [31] B. Kemper, D. Carl, A. Höink, G. Von Bally, I. Bredebusch, and J. Schnekenburger, "Modular digital holographic microscopy system for marker free quantitative phase contrast imaging of living cells," in *Biophotonics and New Therapy Frontiers*, vol. 6191, 61910T-1-8, April 2006.
- [32] Y. Wang, D. Wang, J. Zhao, Y. Yang, X. Xiao, and H. Cui, "Non-invasive monitoring of living cell culture by lensless digital holography imaging," *Chinese Optics Letters*, vol. 9, no. 3, Article ID 030901, 2011.

Research Article

Improved Reconstruction Quality of Bioluminescent Images by Combining SP_3 Equations and Bregman Iteration Method

Qiang Wu, Jinchao Feng, Kebin Jia, and Xiangyu Wang

College of Electronic Information and Control Engineering, Beijing University of Technology, Beijing 100124, China

Correspondence should be addressed to Jinchao Feng; fengjc@bjut.edu.cn

Received 13 September 2012; Accepted 24 December 2012

Academic Editor: Jimin Liang

Copyright © 2013 Qiang Wu et al. This is an open access article distributed under the Creative Commons Attribution License, which permits unrestricted use, distribution, and reproduction in any medium, provided the original work is properly cited.

Bioluminescence tomography (BLT) has a great potential to provide a powerful tool for tumor detection, monitoring tumor therapy progress, and drug development; developing new reconstruction algorithms will advance the technique to practical applications. In the paper, we propose a BLT reconstruction algorithm by combining SP_3 equations and Bregman iteration method to improve the quality of reconstructed sources. The numerical results for homogeneous and heterogeneous phantoms are very encouraging and give significant improvement over the algorithms without the use of SP_3 equations and Bregman iteration method.

1. Introduction

As an emerging molecular imaging technique, bioluminescence imaging (BLI) is potentially well suited for early detection, clinical drug development and monitoring, and regeneration research [1–5]. Therefore, this imaging modality has received increasingly intense research interest worldwide over the recent years.

To date, planar BLI is commonly used because of its ease of implementation and operational simplicity, but it also suffers from significant limitations, including the low resolution, the lack of quantification, and the incapacity of accurately providing depth information [6]. In contrast, bioluminescence tomography (BLT) could overcome these limitations by using accurate reconstruction algorithms coupled with theoretical models of photon propagation in biological tissues, providing higher resolution, quantification accuracy, and depth information [7]. In comparing BLT to planar BLI, planar BLI is a qualitative analysis and BLT is a quantitative analysis [8]. Therefore, scientists are now paying more attention to the advancement of BLT research.

The objective of BLT is to recover the unknown bioluminescent source distribution $s \in \mathbb{R}^n$ based on the noisy surface measurements $\Phi^{\text{meas}} \in \mathbb{R}^m$ [6, 7]. Indeed, the problem is also called the inverse problem. However, a major difficulty in recovering the bioluminescent source distribution is imposed

by multiple scattering which occurs when light propagates through biological tissues. This makes the inverse problem severely ill-posed [7]. Furthermore, the number of recovered unknown source distributions is usually far more than the number of detected boundary measurements, that is, $m < n$ (in many cases, $m \ll n$). Hence, BLT is also a typically underdetermined problem. To obtain a meaningful solution, regularization techniques are usually adopted, which consist of solving the following constrained optimization problem [9]:

$$\min_{s \geq 0} \|As - \Phi^{\text{meas}}\|_2^2 + \lambda \cdot J(s), \quad (1)$$

where $J(\cdot)$ is a properly chosen regularization term, $\lambda > 0$ represents regularization parameter, and $A \in \mathbb{R}^{m \times n}$ is a linear operator, typically formed by discretizing diffusion equation with finite element methods [10].

When $J(s) = \|s\|_2^2$, the above regularized problem becomes the popular Tikhonov regularization, which inherently provides smoothed solutions and therefore offers compromised accuracy in localizing bioluminescent sources [11]. Recently, l_1 -regularized problems, that is, $J(s) = \|s\|_1$, have received an increasing amount of attention in optical imaging, which allow high-quality images to be reconstructed from a small amount of boundary measurements [11–14]. However, l_1 -regularized problems can sparsify the bioluminescent source

distribution, which affects the quality of reconstructed images [13, 15].

Furthermore, in order to obtain the matrix A in (1), the diffusion approximation (DA) to radiative transfer equation (RTE) is widely used as the forward model for BLT reconstructions. Although the DA is one of the most important approximation methods in BLT [6–11], it suffers from some limitations [12–14]. Firstly, the scattering is dominated over absorption and secondly, the DA fails in modeling light propagation in the vicinity of those highly vascularized tissue parts [12–14]. Therefore, the DA will introduce significant error in some BLT cases [14]. In contrast, the RTE is widely accepted as an accurate model for light propagation in biological tissues. However, the use of the RTE as the forward model for BLT is often not feasible due to the facts that analytical solutions cannot exist for biological tissues with spatially nonuniform scattering and absorption properties and the computation of numerical approximations for the solution is extremely time consuming [16, 17]. A generalized delta-Eddington phase function was recently presented to simplify the RTE, and the more accurate solution was obtained relative to the DA [18, 19]. However, the parameter f used in the model is difficult to compute [18, 19]. In addition, the system matrix for the model is also difficult to construct for complex heterogeneous geometries. These factors seriously limit the utilization of the model in BLT. The use of simplified spherical harmonics (SP_N) equations to approximate the RTE has been demonstrated to significantly improve the diffusion solution in domains with high absorption and small geometries [5, 12–14, 16, 20]. Meanwhile, the SP_N methods are computationally less expensive than the RTE ones.

Large efforts in combining multiple types of *a priori* information to develop BLT reconstruction algorithms to improve the quality of reconstructed images, particularly the permissible source region and multispectral information, have formed the grounds of BLT reconstructions [9–11, 20–26]. Despite the recent advances in BLT reconstruction algorithms and light propagation models, it is necessary to develop and refine reconstruction methods to improve image quality.

Bregman iteration method has been studied recently and is widely used in compressed sensing [27, 28]. The idea is to add the residual, that is, the error produced at the current iteration, back to the data for the next iteration to be corrected [27]. The method is particularly attractive for sparse reconstruction, but so far it has not been fully investigated and analyzed in BLT, and this is the goal of this paper.

In this paper, we propose a BLT algorithm to improve the quality of reconstructed images. In the algorithm, SP_3 equations are adapted to model light propagation, and Bregman iteration method is used to solve the inverse problem for BLT. Numerical results demonstrate that the quality of reconstructed images is improved greatly. The rest of the paper is organized as follows. In the following section, we described SP_3 equations as light propagation model and Bregman iteration method. Last, numerical experiments were performed to evaluate the proposed algorithm, and corresponding conclusions were made.

2. Methods

2.1. SP_3 Equations. The propagation of light in biological tissues can be well modeled by SP_3 equations. SP_3 equations are two coupled diffusion equations for the moments ϕ_1 and ϕ_2 [16, 17]:

$$\begin{aligned} -\nabla \cdot \left(\frac{1}{3\mu_{a1}(r)} \nabla \phi_1(r) \right) + \mu_a(r) \phi_1(r) - \frac{2\mu_a(r)}{3} \phi_2(r) &= S(r), \\ -\frac{2\mu_a(r)}{3} \phi_1(r) - \nabla \cdot \left(\frac{1}{7\mu_{a3}(r)} \nabla \phi_2(r) \right) \\ + \left(\frac{4}{9}\mu_a(r) + \frac{5}{9}\mu_{a2}(r) \right) \phi_2(r) &= -\frac{2}{3}S(r), \end{aligned} \quad (2)$$

where $\mu_{an} = \mu_a + (1 - g^m) \cdot \mu_s$ ($m = 1, 2, 3$), and μ_a and μ_s are the absorption and scattering parameters, respectively. g is the anisotropy parameter.

The boundary conditions are given by

$$\begin{aligned} \left(\frac{1}{2} + A_1 \right) \phi_1(r) + \frac{1 + B_1}{3\mu_{a1}(r)} (n \cdot \nabla \phi_1(r)) \\ = \left(\frac{1}{8} + C_1 \right) \phi_2(r) + \frac{D_1}{\mu_{a3}(r)} (n \cdot \nabla \phi_2(r)), \\ \left(\frac{7}{24} + A_2 \right) \phi_2(r) + \frac{1 + B_2}{7\mu_{a3}(r)} (n \cdot \nabla \phi_2(r)) \\ = \left(\frac{1}{8} + C_2 \right) \phi_1(r) + \frac{D_2}{\mu_{a1}(r)} (n \cdot \nabla \phi_1(r)). \end{aligned} \quad (3)$$

The coefficients $A_1, \dots, D_1, \dots, A_2, \dots, D_2$ can be found in [16]. Furthermore, the partial current can be obtained from solutions ϕ_1 and ϕ_2 :

$$\begin{aligned} J^+(r) = \left(\frac{1}{4} + J_0 \right) \phi_1(r) - \frac{0.5 + J_1}{3\mu_{a1}(r)} (n \cdot \nabla \phi_1(r)) \\ + \left(-\frac{1}{16} - \frac{2}{3}J_0 + \frac{1}{3}J_2 \right) \phi_2(r) - \frac{J_3}{7\mu_{a3}(r)} (n \cdot \nabla \phi_2(r)). \end{aligned} \quad (4)$$

The coefficients J_0, J_1, \dots, J_3 can also be found in [16]. Solving the above equations by finite element methods, a linear operator A can be established [29].

2.2. Bregman Iteration Method. Bregman iteration method is based on the definition of Bregman distance. The Bregman distance associated with a convex function E at the point v is given as [27]

$$D_E^p(u, v) = E(u) - E(v) - \langle p, u - v \rangle, \quad (5)$$

where $p \in \partial E$ is in the subgradient of E at v . Clearly, this is not a distance in the usual sense because it is not in general symmetric. However, it does measure closeness in the sense that $D_E^p(u, v) \geq 0$ and $D_E^p(u, v) \geq D_E^p(w, v)$ for w on the line segment between u and v [27].

Initialization: $\varepsilon > 0$, $k_{\max} > 0$, $k = 1$, $v_1 = 0$, and s
 Construct the operator A by solving SP₃ equations
While $\|s_{k+1} - s_k\| / \|s_{k+1}\| < \varepsilon$ or $k < k_{\max}$ **do**
 Solve (7): $s_{k+1} \leftarrow \arg \min_{s \geq 0} \{\|As - (\Phi^{\text{meas}} + v_n)\|_2^2 + \lambda \cdot J(s)\}$
 Update v_k : $v_{k+1} \leftarrow v_k + \Phi^{\text{meas}} - As_{k+1}$
 $k \leftarrow k + 1$
End while

ALGORITHM 1: BLT reconstruction with SP₃ equations and Bregman iteration method.

Based on Bregman iteration method, (1) can be reformulated as

$$\begin{aligned}
 s_{k+1} &= \arg \min_{s \geq 0} D_f^p(s, s_k) + \frac{1}{\lambda} \|As - \Phi^{\text{meas}}\|_2^2 \\
 &= \arg \min_{s \geq 0} \left\{ J(s) - \langle p_k, s - s_k \rangle + \frac{1}{\lambda} \|As - \Phi^{\text{meas}}\|_2^2 \right\}, \\
 p_{k+1} &= p_k - \frac{1}{\lambda} A^T (As_{k+1} - \Phi^{\text{meas}}),
 \end{aligned} \tag{6}$$

where $p_{k+1} \in \partial E(s_{k+1})$ and A^T is the adjoint operator of A . Since the operator A is linear in BLT reconstructions, the above complicated iteration can be transformed to the following two-stage iteration procedure with $v_0 = 0$ [27]:

$$s_{k+1} = \arg \min_{s \geq 0} \{\|As - (\Phi^{\text{meas}} + v_n)\|_2^2 + \lambda \cdot J(s)\}, \tag{7}$$

$$v_{k+1} = v_k + \Phi^{\text{meas}} - As_{k+1}. \tag{8}$$

This is done by iteratively solving the optimization problem (7) and then modifying the measured value of Φ^{meas} used in the next iteration. And (8) is usually referred as ‘‘adding back the noise’’ [30]. In the paper, $J(\cdot)$ is fixed as the l_1 regularizer. The implementation of (7) was performed by a gradient projected (GP) algorithm [31]. The proposed algorithm was depicted in Algorithm 1.

3. Results

To fully evaluate the performance of the proposed algorithm, homogeneous and heterogeneous experiments were performed. In the experiments, the parameters ε and k_{\max} were set to 1×10^{-3} and 10, respectively. The parameters in GP algorithm set default values, except the maximum iteration number is fixed at 50000 to ensure the convergence of the algorithm unless otherwise is specified.

3.1. Homogeneous Phantom Experiments. In this section, 2D numerical simulations were used to investigate the performance of the proposed algorithm since less computational time was required for 2D data. Here, two individual cases were considered. In the first case, numerical simulations were performed on a homogenous circle with 10 mm radius. Within this circle, two sources (source 1 and source 2) were placed in $(-5, 0)$ mm and $(0, 5)$ mm, respectively and each

TABLE 1: Optical properties for different bands [22].

Wavelength	μ_a (mm ⁻¹)	μ_s' (mm ⁻¹)	μ_s'/μ_a	g
600 nm	0.0281	1.6667	59.3	0.9
620 nm	0.0109	1.6129	147.9	0.9

source had a radius of 1.0 mm. The corresponding optical parameters were listed in Table 1. The boundary data were generated for two wavelengths (600 and 620 nm) with finite element methods, and different levels of Gaussian noise (0%, 10%, and 30%) were added to the datasets. BLT reconstructions were performed without and with Bregman iteration method. Corresponding results were shown in Figure 1. In this case, the ratios of μ_s'/μ_a are larger than 10; therefore, the circular phantom has high-scattering characteristics. Hence, the DA is suitable for the simulation. For comparison, we carried out BLT reconstructions with the DA as the forward model; reconstructed images were also illustrated in Figure 1. From Figure 1, we can see that the results with SP₃ equations are better than those obtained with the DA and Bregman iteration method can improve the quality of reconstructed images. The best results are obtained by combining SP₃ equations and Bregman iteration method. In addition, quantitative results were summarized in Table 2. Data in Table 2 show that reconstructed position errors can be significantly reduced when SP₃ equations are used together with Bregman iteration method

Furthermore, we tested the proposed algorithm by using experiments with multiple bioluminescent sources. The optical properties of a real mouse muscle for different wavelengths (580 and 620 nm) were assigned as listed in Table 3 [29]. Four identical sources with 1 mm radii were placed different positions. First, the sources were placed near the surfaces, and the distance to the center of the circle was 7.07 mm. The boundary measurements were also produced by finite element methods, and 20% Gaussian noise was added into the simulated data. Note that in the test, μ_s'/μ_a for two wavelengths are less than 10; therefore, the condition $\mu_s' \gg \mu_a$ does not hold and the DA is less valid. Hence, BLT reconstructions with the DA were not implemented. The results with SP₃ equations are shown in Figures 2(a) and 2(b). Next, the sources were placed at 5 mm positions off the center. Then BLT reconstructions were performed, as shown in Figures 2(c) and 2(d). Furthermore, quantitative results were shown in Table 4. It is worthy of mentioning

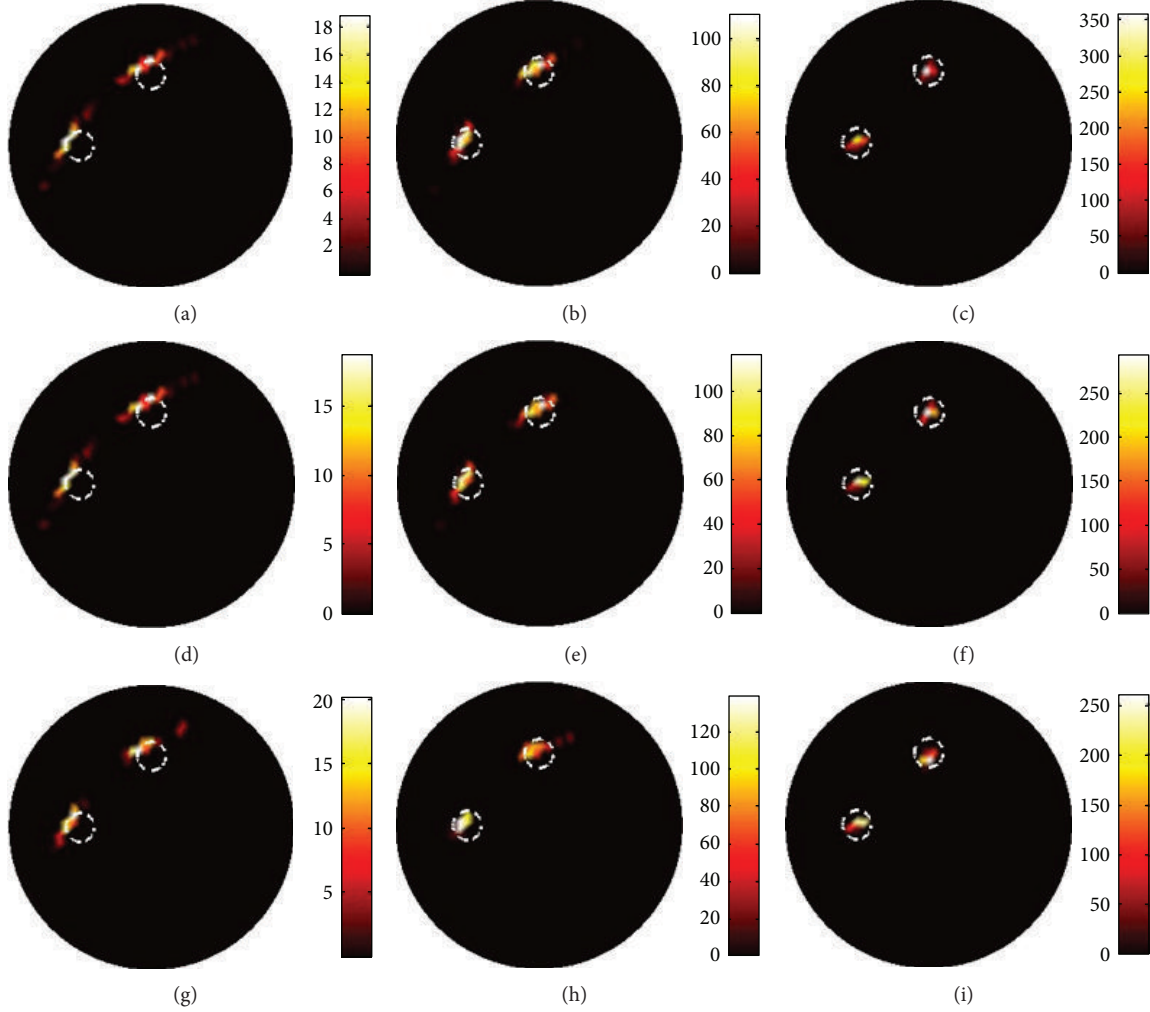


FIGURE 1: Reconstructed images with different methods with different levels of noisy data. The first and second columns are reconstructed results with the DA and SP_3 equations as the forward models, respectively. The last column is the images by combing SP_3 equations and Bregman iteration method. The first row is the results with noise-free data and the middle and last rows are the results with 10% and 30% noisy data. The white circles represent the actual sources.

TABLE 2: Quantitative reconstruction results in the case of two sources for homogeneous phantom experiments.

Noise levels	Number of source	Reconstructed central position using different methods (unit: mm)		
		DA	SP_3	SP_3 + Bregman
0%	No. 1	(-5.99, 0.35)	(-5.49, 0.28)	(-5.00, 0.21)
	No. 2	(-0.08, 6.00)	(0.14, 5.50)	(-0.15, 5.00)
10%	No. 1	(-5.99, 0.35)	(-5.49, 0.28)	(-5.00, 0.21)
	No. 2	(-0.08, 6.00)	(0.14, 5.50)	(-0.15, 5.00)
30%	No. 1	(-5.45, 0.78)	(-5.49, 0.28)	(-5.00, 0.21)
	No. 2	(-0.86, 5.43)	(-0.64, 4.96)	(0.07, 4.50)

that BLT reconstructions without and with Bregman iteration method use the same regularization parameter (i.e., 3×10^{-6}), but the reconstructed results are different. From Figure 2 and Table 4, it is easily concluded that better images can be obtained by combining SP_3 equations and Bregman iteration method.

3.2. Heterogeneous Phantom. In the subsection, a micro-MRI-based heterogeneous mouse model (MOBY) was used to validate the proposed algorithm [32]. About 2/3 of the entire phantom was used for mesh generation, and a volumetric mesh with 17661 nodes and 93312 tetrahedron elements was obtained by iso2mesh [33], as shown in Figure 3.

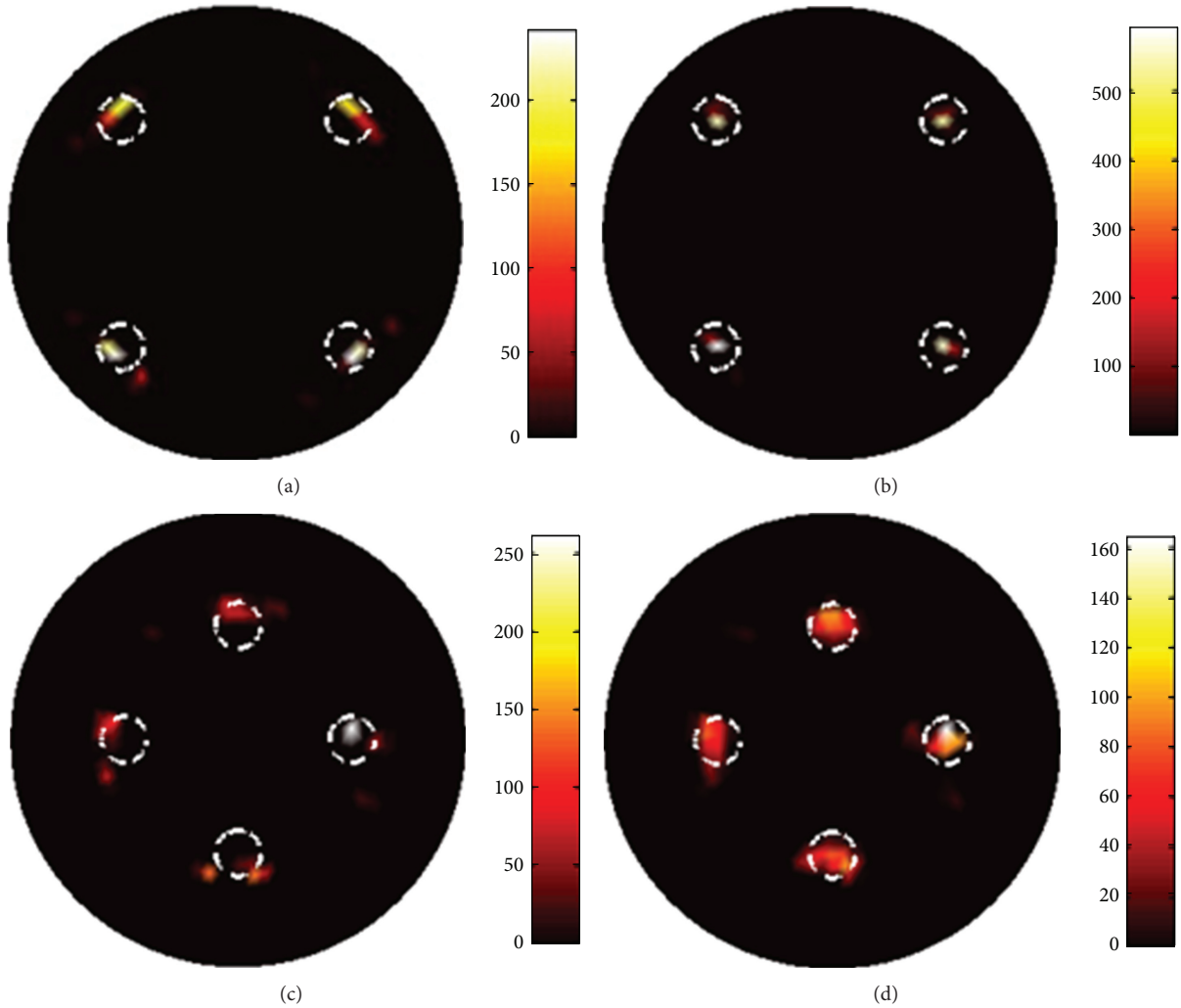


FIGURE 2: Reconstructed images in the case of four sources. The corresponding images are shown for sources near the surfaces (top row) and near the center (bottom row). (a) and (c) are results obtained only with SP_3 equations. (b) and (d) are the results by combining SP_3 equations and Bregman iteration method.

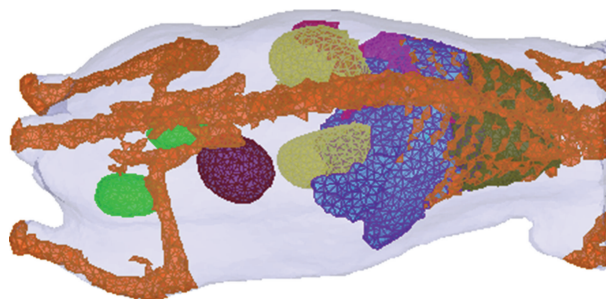


FIGURE 3: The heterogeneous mouse phantom.

The optical properties of different tissues were assigned according to Table 5, reproduced from Alexandrakis et al. [21]. The forward simulation data was produced by finite element methods, and 10% Gaussian noise was added. Then BLT reconstructions were performed without and with Bregman iteration method. The regularization parameters used in

the two methods were the same, and the value was 0.1. The maximum iteration number in the GP algorithm was set to 5000, and other parameters remained unchanged. The reconstructed results without and with Bregman iteration method were shown in Figure 4. From the images, we can see that the quality of reconstructed images can be improved with the

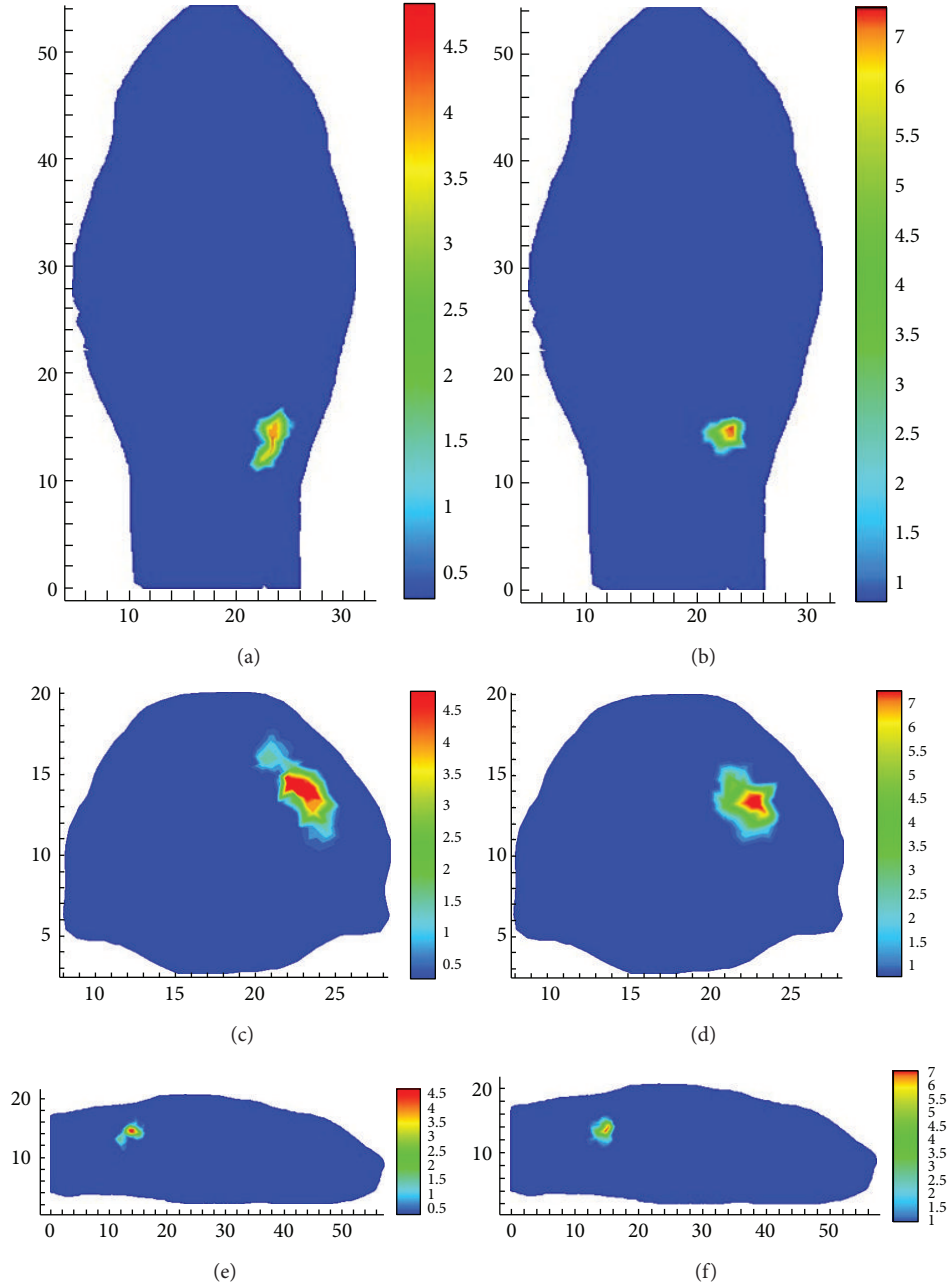


FIGURE 4: Cross sections of the reconstructed images through the actual center of the real source for heterogeneous mouse experiment. (a) and (b) are coronal sections; (c) and (d) transverse sections; (e) and (f) sagittal sections. The first and second columns show reconstructions without and with Bregman iteration method, respectively.

TABLE 3: Optical property parameters used in the case four sources [29].

Wavelength	μ_a (mm^{-1})	μ_s (mm^{-1})	μ_s'/μ_a	g
580 nm	0.463	9.75	2.11	0.9
620 nm	0.107	9.22	8.62	0.9

use of Bregman iteration method. Furthermore, the reconstructed central positions for the two algorithms are (22.77, 14.95, 13.33 mm) and (22.24, 13.95, 14.49 mm), respectively.

The real source position is (22.07, 14.43, 13.06 mm). The absolute distances between reconstructed sources and the real source are 0.91 mm and 1.52 mm, respectively. The quantitative results also demonstrate that Bregman iteration method can improve the quality of reconstructed images.

4. Conclusion

We have presented a BLT reconstruction algorithm by combining SP_3 equations and Bregman iteration method as a competitive method for reconstructing bioluminescent sources

TABLE 4: Quantitative results between the actual and the reconstructed source centers with different methods in the case of four sources.

Actual source position	Reconstructed source position with SP ₃ method	Reconstructed source position with SP ₃ and Bregman method
(5, -5)	(5.14, -5.47)	(4.96, -4.94)
(-5, -5)	(-5.27, -5.34)	(-4.94, -4.96)
(-5, 5)	(-4.81, 5.76)	(-4.95, 4.95)
(5, 5)	(4.86, 5.72)	(4.95, 4.95)
(5, 0)	(4.98, 0.50)	(4.98, 0.50)
(-5, 0)	(-5.45, 0.78)	(-5.49, 0.28)
(0, 5)	(-0.36, 5.49)	(0.14, 5.50)
(0, -5)	(0.72, -5.96)	(0.58, -5.47)

TABLE 5: Optical properties of biological tissues for different wavelengths [21].

	620 nm			700 nm		
	μ_a (mm ⁻¹)	μ_s (mm ⁻¹)	g	μ_a (mm ⁻¹)	μ_s (mm ⁻¹)	g
Muscle	0.086	4.29	0.9	0.0027	11.8	0.9
Skeleton	0.06	24.95	0.9	0.039	23.4	0.9
Heart	0.058	9.63	0.9	0.038	9.05	0.9
Bladder	0.086	4.29	0.9	0.0027	11.8	0.9
Testis	0.086	4.29	0.9	0.043	21.09	0.9
Pancreas	0.345	6.78	0.9	0.23	6.48	0.9
Spleen	0.345	6.78	0.9	0.0077	13.77	0.9
Stomach	0.086	4.29	0.9	0.23	6.48	0.9
Liver	0.345	6.78	0.9	0.043	21.09	0.9
Kidneys	0.05	5.4	0.9	0.23	6.48	0.9
Lungs	0.195	21.73	0.9	0.13	21.24	0.9

and validated the proposed algorithm using homogeneous and heterogeneous experiments. It has been demonstrated that the proposed algorithm can enhance the recovery of bioluminescent sources in terms of the quality of reconstructed images and localization error.

The use of SP₃ equations is a helpful technique to improve BLT reconstructions. Our experiments have illustrated that the appearance of artifacts can be reduced when SP₃ equations are used as the forward model. However, the computation of the system matrix A by solving SP₃ equations is very expensive, especially when the imaged objects are very complex, irregular, and heterogeneous. Fortunately, with the fast development of graphics processing unit (GPU), the computation of A can be significantly accelerated.

One merit of the proposed algorithm is that the improved results are obtained by making use of the available boundary measurements and thus do not require increased number of boundary measurements and do not bring more hardware requirements. Meanwhile, the proposed algorithm is relatively easy to implement. Therefore, the algorithm is suitable for *in vivo* applications. As a sacrifice, the computational burden for the proposed algorithm is greatly increased, especially for the heterogeneous mouse experiment, since solving (1) brings extra cost through Bregman iteration method, and each iteration of which is equivalent of solving a standard “L1” problem. To increase computational efficiency

for mouse experiments, developing fast large-scale optimization algorithms is essential.

In conclusion, we have developed a BLT reconstruction algorithm by combing SP₃ equations and Bregman iteration method and indicated its feasibility and merits. In the near future, we expect to accelerate the proposed algorithm based on GPU and extend it to *in vivo* mouse experiments.

Acknowledgments

This paper is supported by the National Natural Science Foundation of China under Grant nos. 30970780 and 81000624, the Science and Technology Key Project of Beijing Municipal Education Commission under Grant no. KZ200910005005, the Doctoral Fund of the Ministry of Education of China under Grant no. 20091103110005, the Rixin Fund of Beijing University of Technology under Grant no. 2013-RX-L04”, and the Scientific Research Fund of Beijing University of Technology under Grant no. X0002012201101.

References

- [1] V. Ntziachristos, J. Ripoll, L. V. Wang, and R. Weissleder, “Looking and listening to light: the evolution of whole-body photonic imaging,” *Nature Biotechnology*, vol. 23, no. 3, pp. 313–320, 2005.

- [2] R. Weissleder and M. J. Pittet, "Imaging in the era of molecular oncology," *Nature*, vol. 452, no. 7187, pp. 580–589, 2008.
- [3] J. K. Willmann, N. van Bruggen, L. M. Dinkelborg, and S. S. Gambhir, "Molecular imaging in drug development," *Nature Reviews Drug Discovery*, vol. 7, no. 7, pp. 591–607, 2008.
- [4] T. Schroeder, "Imaging stem-cell-driven regeneration in mammals," *Nature*, vol. 453, no. 7193, pp. 345–351, 2008.
- [5] J. Feng, C. Qin, K. Jia, S. Zhu, X. Yang, and J. Tian, "Bioluminescence tomography imaging *in vivo*: recent advances," *IEEE Journal of Selected Topics in Quantum Electronics*, vol. 18, no. 4, pp. 1394–1402, 2012.
- [6] X. Gu, Q. Zhang, L. Larcom, and H. Jiang, "Three-dimensional bioluminescence tomography with model-based reconstruction," *Optics Express*, vol. 12, no. 17, pp. 3996–4000, 2004.
- [7] G. Wang, Y. Li, and M. Jiang, "Uniqueness theorems in bioluminescence tomography," *Medical Physics*, vol. 31, no. 8, pp. 2289–2299, 2004.
- [8] G. Wang, H. Shen, W. Cong, S. Zhao, and G. W. Wei, "Temperature-modulated bioluminescence tomography," *Optics Express*, vol. 14, no. 17, pp. 7852–7871, 2006.
- [9] S. Ahn, A. J. Chaudhari, F. Darvas, C. A. Bouman, and R. M. Leahy, "Fast iterative image reconstruction methods for fully 3D multispectral bioluminescence tomography," *Physics in Medicine and Biology*, vol. 53, no. 14, pp. 3921–3942, 2008.
- [10] W. Cong, G. Wang, D. Kumar et al., "Practical reconstruction method for bioluminescence tomography," *Optics Express*, vol. 13, no. 18, pp. 6756–6771, 2005.
- [11] Y. Lu, X. Zhang, A. Douraghy et al., "Source reconstruction for spectrally-resolved bioluminescence tomography with sparse a priori information," *Optics Express*, vol. 17, no. 10, pp. 8062–8080, 2009.
- [12] H. Gao and H. Zhao, "Multilevel bioluminescence tomography based on radiative transfer equation part 1: l1 regularization," *Optics Express*, vol. 18, no. 3, pp. 1854–1871, 2010.
- [13] H. Gao and H. Zhao, "Multilevel bioluminescence tomography based on radiative transfer equation part 2: total variation and l1 data fidelity," *Optics Express*, vol. 18, no. 3, pp. 2894–2912, 2010.
- [14] K. Liu, J. Tian, C. Qin et al., "Tomographic bioluminescence imaging reconstruction via a dynamically sparse regularized global method in mouse models," *Journal of Biomedical Optics*, vol. 16, no. 4, Article ID 046016, 2011.
- [15] J. Feng, C. Qin, K. Jia et al., "Total variation regularization for bioluminescence tomography with the split Bregman method," *Applied Optics*, vol. 51, no. 19, pp. 4501–4512, 2012.
- [16] A. D. Klöse and E. W. Larsen, "Light transport in biological tissue based on the simplified spherical harmonics equations," *Journal of Computational Physics*, vol. 220, no. 1, pp. 441–470, 2006.
- [17] Z. Yuan, X. H. Hu, and H. Jiang, "A higher order diffusion model for three-dimensional photon migration and image reconstruction in optical tomography," *Physics in Medicine and Biology*, vol. 54, no. 1, pp. 65–88, 2009.
- [18] W. Cong, A. Cong, H. Shen, Y. Liu, and G. Wang, "Flux vector formulation for photon propagation in the biological tissue," *Optics Letters*, vol. 32, no. 19, pp. 2837–2839, 2007.
- [19] W. Cong, H. Shen, A. Cong, Y. Wang, and G. Wang, "Modeling photon propagation in biological tissues using a generalized Delta-Eddington phase function," *Physical Review E*, vol. 76, no. 5, Article ID 051913, 2007.
- [20] A. D. Klöse, B. J. Beattie, H. Dehghani et al., "In vivo bioluminescence tomography with a blocking-off finite-difference SP₃ method and MRI/CT coregistration," *Medical Physics*, vol. 37, no. 1, pp. 329–338, 2010.
- [21] G. Alexandrakakis, F. R. Rannou, and A. F. Chatziioannou, "Tomographic bioluminescence imaging by use of a combined optical-PET (OPET) system: a computer simulation feasibility study," *Physics in Medicine and Biology*, vol. 50, no. 17, pp. 4225–4241, 2005.
- [22] H. Dehghani, S. C. Davis, S. Jiang, B. W. Pogue, K. D. Paulsen, and M. S. Patterson, "Spectrally resolved bioluminescence optical tomography," *Optics Letters*, vol. 31, no. 3, pp. 365–367, 2006.
- [23] Y. Lv, J. Tian, W. Cong et al., "A multilevel adaptive finite element algorithm for bioluminescence tomography," *Optics Express*, vol. 14, no. 18, pp. 8211–8223, 2006.
- [24] J. Feng, K. Jia, G. Yan et al., "An optimal permissible source region strategy for multispectral bioluminescence tomography," *Optics Express*, vol. 16, no. 20, pp. 15640–15654, 2008.
- [25] J. Feng, K. Jia, C. Qin et al., "Three-dimensional bioluminescence tomography based on Bayesian approach," *Optics Express*, vol. 17, no. 19, pp. 16834–16848, 2009.
- [26] J. Feng, C. Qin, K. Jia et al., "An adaptive regularization parameter choice strategy for multi-spectral bioluminescence tomography," *Medical Physics*, vol. 38, no. 11, pp. 5933–5944, 2011.
- [27] T. Goldstein and S. Osher, "The split Bregman method for l1-regularized problems," *SIAM Journal on Imaging Sciences*, vol. 2, no. 2, pp. 323–343, 2009.
- [28] S. Osher, Y. Mao, B. Dong, and W. Yin, "Fast linearized Bregman iteration for compressive sensing and sparse denoising," *UCLA CAM Reports 08-37*, 2008.
- [29] Y. Lu, A. Douraghy, H. B. Machado et al., "Spectrally resolved bioluminescence tomography with the third-order simplified spherical harmonics approximation," *Physics in Medicine and Biology*, vol. 54, no. 21, pp. 6477–6493, 2009.
- [30] S. Osher, M. Burger, D. Goldfarb, J. Xu, and W. Yin, "An iterative regularization method for total variation-based image restoration," *Multiscale Modeling and Simulation*, vol. 4, no. 2, pp. 460–489, 2005.
- [31] M. A. T. Figueiredo, R. D. Nowak, and S. J. Wright, "Gradient projection for sparse reconstruction: application to compressed sensing and other inverse problems," *IEEE Journal on Selected Topics in Signal Processing*, vol. 1, no. 4, pp. 586–597, 2007.
- [32] W. P. Segars, B. M. W. Tsui, E. C. Frey, G. A. Johnson, and S. S. Berr, "Development of a 4-D digital mouse phantom for molecular imaging research," *Molecular Imaging and Biology*, vol. 6, no. 3, pp. 149–159, 2004.
- [33] Q. Fang and D. A. Boas, "Tetrahedral mesh generation from volumetric binary and grayscale images," in *Proceedings of the IEEE International Symposium on Biomedical Imaging: From Nano to Macro (ISBI '09)*, pp. 1142–1145, Boston, Mass, USA, July 2009.